Effect of wind speed on marine aerosol optical properties over remote oceans with use of spaceborne lidar observations

Kangwen Sun[1], Guangyao Dai[1], Songhua Wu[1, 2, 3], Oliver Reitebuch[4], Holger Baars[5], Jiqiao Liu[6], Suping Zhang[7]

[1]College of Marine Technology, Faculty of Information Science and Engineering, Ocean University of China, 266100 Qingdao, China
[2]Laoshan Laboratory, 266237 Qingdao, China
[3]Institute for Advanced Ocean Study, Ocean University of China, 266100 Qingdao, China
[4]Institut für Physik der Atmosphäre, Deutsches Zentrum für Luft- und Raumfahrt e.V. (DLR), 82234 Oberpfaffenhofen, Germany
[5]Leibniz Institute for Tropospheric Research (TROPOS), 04318 Leipzig, Germany
[6]Laboratory of Space Laser Engineering, Shanghai Institute of Optics and Fine Mechanics, Chinese Academy of Sciences, 201800 Shanghai, China
[7]Physical Oceanography Laboratory, Ocean University of China, 266100 Qingdao, China

Correspondence to: Guangyao Dai (daiguangyao@ouc.edu.cn)

Abstract. In this paper, using Aeolus data, the relationships between the marine aerosol optical properties at 355 nm and the corresponding instantaneous co-located wind speeds of three remote ocean areas are investigated and analysed at two separate vertical atmospheric layers (0-1 km and 1-2 km, corresponding to the heights within and above marine atmospheric boundary layer (MABL)), revealing the effect of wind speed on marine aerosol over the remote ocean. Marine aerosol extinction/backscatter coefficients and background wind speeds show positive relationships. Their correlations are modeled using power-law functions, with corresponding R^2 values all greater than 0.9. Both the MABL and the layer above it receive the marine aerosol produced and transported by the wind from the sea-air interface. The marine aerosol load in the lower layer (MABL) is stronger than in the higher layer. The intensity of marine aerosol extinction/backscatter coefficients enhancements caused by the background wind is greater in the MABL. The slope variation points occur during the marine aerosol extinction/backscatter coefficients increasing with wind speed. Above these points, the growth rate decreases. This may indicate that the wind-driven enhancement of marine aerosol involves two phases: a rapid growth phase with high wind dependence, followed by a slower growth phase after the slope variation points. The correlation between the marine aerosol optical depth at 355 nm and the corresponding wind speeds is established, and verified by comparing it with CALIPSO-derived results from previous research. The variation of the marine aerosol lidar ratio at 355 nm with wind speed is also examined, suggesting a possible increasing-decreasing-increasing trend of marine aerosol particle size as wind speed increases.

1 Introduction

According to the Intergovernmental Panel on Climate Change (IPCC) Fifth Assessment Report, the total emission of marine aerosol (including marine primary organic aerosol) produced from ocean is 1400 to 6800 $Tg \cdot yr^{-1}$, which is considered the largest natural aerosol input to the atmosphere globally (Boucher et al., 2013). Accurate estimation of marine aerosol production, evolution and dissipation, and the knowledge of marine aerosol spatial and temporal distribution are significant for studying the global energy budget, aerosol-cloud interactions and visibility changes (Latham and Smith, 1990; Murphy et al., 1998; O'Dowd et al., 1999; Haywood et al., 1999; de Leeuw et al., 2000; Kaufman et al., 2002; Smirnov et al., 2012). Radiative forcing caused by marine aerosol is a significant contributor to the global energy budget. It was reported that the average marine aerosol optical depth (AOD_{mar}) is approximately 0.15 while the volume concentration of cloud condensation nuclei from marine aerosol is around 60 cm^{-3} (Kaufman et al., 2002; Lewis and Schwartz, 2004). Therefore, marine aerosol has both direct and indirect impacts on radiative forcing, which are scattering and absorbing solar radiation, and converting cloud microphysical properties, respectively (Murphy et al., 1998; Pierce and Adams, 2006). The knowledge of the impact of the magnitude and changes of marine aerosol emissions on the shifts in climate and marine ecosystem processes is limited (IPCC, 2021).

Marine aerosols mainly include primary sea spray particles and secondary aerosols produced by the oxidation of emitted precursors. Sea spray particles, composed of sea-salt and primary organic aerosols, are produced by wind induced wave breaking as well as the wind driving direct mechanical disruption of waves crests (O'Dowd and de Leeuw, 2007; IPCC, 2021). Moreover, as a dynamical meteorological factor, wind speed also has vital influence on the transport, evolution and dissipation of aerosols. Consequently, the wind speed is a crucial factor which governs the production and life cycle of marine aerosol (Lewis and Schwartz, 2004). Exploring the accurate relationships between marine aerosol optical properties (aerosol optical depth (AOD), extinction coefficient (α), backscatter coefficient (β), etc.) and wind speed are significant for improving global aerosol transport models (Jaegle et al., 2011; Madry et al., 2011; Fan and Toon, 2011), for enhancing satellite-retrieved AODs (Kahn et al., 2010; Kleidman et al., 2012), for atmospheric correction of ocean color (Zibordi et al., 2011) and for the study of biogeochemical cycles (Meskhidze and Nenes, 2010). Several efforts have been reported to explore the relationship between the AOD or aerosol extinction coefficient over the ocean and wind speed. Utilizing either satellite-retrieved AODs (Glantz et al., 2009; Huang et al., 2010; Lehahn et al., 2010; O'Dowd et al., 2010; Grandey et al., 2011) or surface (coast, island or ship)-based measurement AODs (Platt and Patterson, 1986; Villevalde et al., 1994; Smirnov et al., 1995; Wilson and Forgan, 2002; Smirnov et al., 2003; Shinozuka et al., 2004; Mulcahy et al., 2008; Lehahn et al., 2010; Adames et al., 2011; Sayer et al., 2012; Smirnov et al., 2012), major previous researches focused on the AOD measured by passive instruments (mainly sun-photometer). From these studies, various power-law or linear relationships revealing positive correlation between AODs over the ocean and surface wind speed were established. The passive instruments lack the abilities of distinguishing marine aerosol from other aerosols, acquiring vertical profiles of aerosols, and retrieving aerosol optical properties without sunlight (except for lunar-photometer) and under cloudy conditions

(Kiliyanpilakkil and Meskhidze, 2011; Winker and Pelon, 2003). Active optical instruments for aerosol measurements, mainly like lidar, were also used in revealing the relationship between AOD/extinction coefficient of marine aerosol and wind speed. A shipborne depolarization lidar was occupied to acquire aerosol extinction coefficients over the East Sea of Korea near Busan and Pohang, associated with the measurement of an anemometer mounted on a mast, finding a positive linear relationship (R^2 =0.57) between extinction (532 nm) at 300 ± 50 m and wind speed at 20 m (Shin et al., 2014). However, this relationship was established with data offshore thus it can not be representative for the global ocean. Cloud-Aerosol Lidar with Orthogonal Polarization (CALIOP) onboard Cloud-Aerosol Lidar and Infrared Pathfinder Satellite Observation (CALIPSO) mission is capable of measuring the global aerosol optical properties vertical distributions and recognizing aerosol types (include "clean marine"). Kiliyanpilakkil and Meskhidze (2011) selected CALIOP-retrieved pure AOD_{mar} below 2 km over ocean by utilizing the CALIOP aerosol subtype products and combined them with the surface wind speed provided by the Advanced Microwave Scanning Radiometer (AMSR-E) on board the Aqua satellite, acquiring a relatively complex increasing regression function, which will be presented and compared in Section 4.4.2 of this paper. Besides, Prijith et al. (2014) also made use of CALIOP-retrieved AODs below 0.5 km over ocean and the surface wind speed, obtaining nearly positive correlation linear relationships. Nevertheless, the assumed marine aerosol lidar ratio (LR_{mar}) (20 sr at 532nm) is used in the AOD_{mar} retrieval process of CALIOP (Kiliyanpilakkil and Meskhidze, 2011), but the LR_{mar} can vary from 10 sr to around 40 sr at 532 nm (Groß et al., 2013; Groß et al., 2015; Bohlmann et al., 2018; Floutsi et al., 2023), which could generate deviations during the retrieval of AOD_{mar} . In summary, to explore the accurate relationship between the marine aerosol optical properties and the wind speed, it is essential to conduct global continuous observations and obtain the information of aerosol type identification, while vertical profiles of aerosols can provide extra spatial information for further analysis. Moreover, previous studies mostly focused on the layer AOD_{mar} and ocean surface wind speed, exploring the probable production of marine aerosol driven by surface wind. The relationship between the vertical marine aerosol optical properties and the corresponding spatiotemporally synchronous wind speed is still to be investigated, which represents the marine-atmospheric background state and may reveal the transport and evolution of the marine aerosol vertically.

The Atmospheric Laser Doppler Instrument (ALADIN), the first-ever spaceborne direct detection wind lidar, was the unique payload installed on the Aeolus satellite mission of the European Space Agency (ESA), which was launched into space in August 2018 (Stoffelen et al., 2005; Reitebuch et al., 2012; Kanitz et al., 2019). As a direct detection high-spectral-resolution lidar, ALADIN has the capability in providing the global aerosol optical properties (e.g., α and β) profiles at 355 nm (Level 2A product), the horizontal-line-of-sight (HLOS) wind speed profiles (Level 2B product), and the wind vector profile from the European Centre for Medium-Range Weather Forecasts (ECMWF) model along the Aeolus track (Level 2C product) (Rennie et al., 2020). It should be emphasized that the aerosol and wind product are retrieved from the backscattered signal of the same laser light pulse emitted from ALADIN to the atmosphere, hence the geolocation and time information of these products is completely consistent for every profile. The detection altitude range of these products is

from the earth surface to around 20 km and the vertical resolutions varies from 0.25 km to 2 km (from bottom to top). Though regarded as a by-product, the particle optical property products are still demonstrated to provide valuable information about particles, especially on the detection and characterization of aerosol and cloud layers and on the lidar ratios (LRs) (Baars et al., 2021; Flament et al., 2021; Abril-Gago et al., 2022). Dai et al. (2022) conducted the first attempt on the combined application of the aerosol products (Level 2A products) and the wind vector products (Level 2C products) of ALADIN, observing an enormous dust transport event occurred in June 2020 from the Sahara to the Americas, describing the transport quantitatively by calculating dust advection.

As mentioned above, Aeolus can provide global high spatial and temporal resolution aerosol optical properties profiles and wind speed profiles. Additionally, CALIOP can provide global aerosol types information. Hence, the combination of Aeolus-CALIOP products is capable of analysing the relationship between the marine aerosol optical properties (e.g., α, β, LR) at 355 nm and wind speed globally and vertically. In this paper, by utilizing Aeolus Level 2A, Level 2C products and CALIOP aerosol subtype products, we firstly 1) select ocean areas far from land and examine the domination of marine aerosol over these areas with the CALIOP aerosol classification products, and then 2) try to acquire the pure marine aerosol optical properties (α, β, LR) at 355 nm and the corresponding wind speeds from Aeolus products, and to analyse the spatial distributions of those atmospheric state parameters at two separate vertical layers (0 km to 1 km, 1 km to 2 km, corresponding to the layers within and above the marine atmospheric boundary layer (MABL), respectively), and finally 3) explore the relationship between the marine aerosol optical properties and the wind speeds vertically above ocean. Generally, the highlights of this work mainly include 1) acquiring the spatiotemporally synchronous relationship between the aerosol optical properties (α, β, LR) and the instantaneous wind speeds, which could indicate the background atmosphere states within and above the MABL over remote ocean, 2) conducting analysis at two separate height layers above ocean surface to explore the vertical differences in aspect of the wind-drive marine aerosol evolution.

The paper is organized as follows: section 2 introduces the spaceborne lidars and their specific products used in this study; section 3 provides the methodology of study areas selection, data pre-processing and data analyses for relationship exploration between marine aerosol optical properties and wind speed; section 4 presents the procedure of study areas selection, then analyses and discusses the marine aerosol optical properties, the wind speed, and their relationship above three selected areas.

2 Spaceborne lidars and products

2.1 ALADIN/Aeolus

Since its launch in August 2018, ALADIN, has been globally observing the profiles of the component of the wind vector along the laser's line of sight (LOS), and the profiles of aerosol optical properties, for more than four years. Aeolus flies at a mean altitude of about 320 km in a sun-synchronous orbit with the local equatorial crossing time of about 06:00 and 18:00, a

daily quasi-global coverage (about 16 orbits per day) with an orbit repeat cycle of 1 week (111 orbits) (Reitebuch, 2012). Designed as a high-spectral-resolution lidar with a laser wavelength of 354.8 nm, ALADIN has the ability to acquire wind profiles and particle optical properties simultaneously with its two separate optical frequency discrimination channels named as Rayleigh channel and Mie channel. The detailed descriptions of the instrument design and the measurement concept are introduced in, e.g., Ansmann et al. (2007), Dabas et al. (2008), Flamant et al. (2008), Reitebuch (2012), Lux et al. (2020) and Flament et al. (2021).

Processed in different phases, Aeolus data products are classified at several levels: Level 0 (instrument housekeeping data), Level 1B (engineering-corrected HLOS winds), Level 2A (aerosol and cloud layer optical properties), Level 2B (meteorologically representative HLOS winds) and Level 2C (Aeolus-assisted wind vectors) (Flamant et al., 2008; Tan et al.,2008; Rennie et al., 2020). It should be emphasized that Level 2C wind vectors are the outputs from the assimilation of the Aeolus Level 2B products in the ECMWF numerical weather prediction (NWP) operational model after 9 January 2020 (Rennie et al., 2021). In addition, the products of Aeolus are available into different Baselines which correspond to different processor versions used to derive the products. The products were firstly released as Baseline 07 at the beginning and updated to Baseline 14 until this study is conducted. As mentioned above, we use Level 2A and Level 2C products of Aeolus for the study of the relationship between marine aerosol optical properties and wind speeds. As the because Level 2C products can provide both components of the wind vector that we use Level 2C instead of Level 2B products of Aeolus. The time coverage of Aeolus products used in this study is from 20 April 2020 to 4 July 2022. Thus, in the aspect of the utilized Level 2A products, the data processors are Baseline 11 (20 April 2020 to 26 May 2021), Baseline 12 (26 May 2021 to 6 December 2021), Baseline 13 (6 December 2021 to 29 March 2022) and Baseline 14 (29 March 2022 to 4 July 2022), while as for the Level 2C products, the data processors are Baseline 09 (20 April 2020 to 9 July 2020), Baseline 10 (9 July 2020 to 8 October 2020), Baseline 11 (8 October 2020 to 26 May 2021), Baseline 12 (26 May 2021 to 6 December 2021), Baseline 13 (6 December 2021 to 29 March 2022) and Baseline 14 (29 March 2022 to 4 July 2022), respectively (https://aeolus-ds.eo.esa.int/oads/access/, last access: 16 February 2023). The Level 2C NWP wind vector products from ECMWF used in this study are obtained after assimilation of the Level 2B observed HLOS wind products.

2.2 CALIOP/CALIPSO

CALIOP, one of the payloads installed on CALIPSO, has been measuring global vertical aerosol and cloud optical properties profiles for more than 16 years since 2006. It can provide α at 532 nm and 1064 nm, β at 532 nm and 1064 nm, depolarization ratio at 532 nm, vertical feature mask (VFM) products and so on (Winker et al., 2009). The VFM products comprise the vertical information along every profile on the identification of clouds and aerosols, and further, on the subtype classification of clouds and aerosols. For cloud and aerosols identification, the cloud-aerosol discrimination (CAD) algorithm is applied based on layer-integrated volume depolarization ratio, layer-integrated total attenuated color ratio, layer-mean attenuated backscatter at 532 nm, latitude and altitude (Liu et al., 2019). The aerosol sub-types are distinguished as “marine”, “dusty marine”, “dust”, “polluted dust”, “continental”, “polluted continental”, “elevated smoke” and “others” via

the joint analysis of particulate depolarization ratio, integrated attenuated backscatter coefficient at 532 nm, layer top altitude, layer base altitude and surface type (Kim et al., 2018). In this study, CALIOP Level (L2) VFM products are applied to confirm the domination of the marine aerosol over the selected ocean areas. Different versions of the CALIOP L2 VFM product are used, respectively, the versions are 4.10 (20 April 2020 to 1 July 2020), 4.20 (1 July 2020 to 19 January 2022) and 3.41 (19 January 2022 to 4 July 2022).

3 Methodology

In general, the data processing and analysis procedure of this study can be concluded briefly as three parts including selection of the study areas, data pre-processing and data analyses, respectively. The flowchart of the study methodology is shown as Fig. 2.

Firstly, this work mainly focuses on the marine aerosol, hence the ocean areas for the study are supposed to be far away from land to reduce the influence of terrestrial aerosols, e.g. anthropogenic, dust, biomass burning. In this work, we selected three ocean areas located in the North Pacific ocean, South Pacific ocean, South Indian ocean, with the latitude and longitude range of 0 ° to 30 ° N and 150 ° E to 180 ° to 150 ° W, 20 ° S to 60 ° S and 100 ° W to 150 ° W, 20 ° S to 60 ° S and 60 ° E to 90 ° E, respectively, as shown in Fig. 1. Hence, we call these three remote ocean areas “the NP area”, “the SP area” and “the SI area” in this paper, respectively.

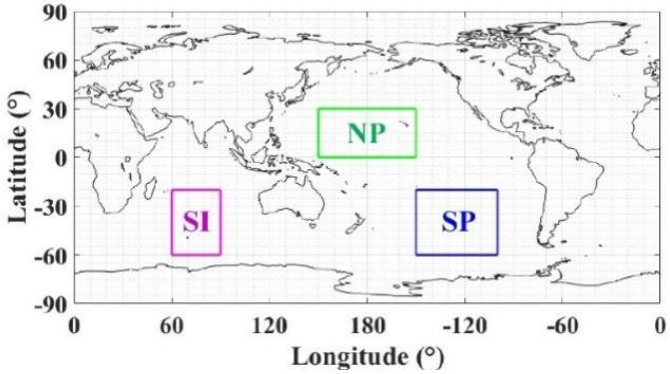

Figure 1: The selected study ocean areas.

The aerosol classification information from CALIOP VFM products are utilized to statistically analyse the aerosol types of the selected areas. It is found that the marine aerosols are mostly distributed at the altitude range of 0 km to 2 km during the VFM processing. Therefore, the statistical analysis of aerosol types is conducted at the same altitude range. It is considered that the marine aerosol dominates in the selected area if the percentage of aerosol subtype “marine” is larger than 75% meanwhile the percentage sum of “marine” and “dusty marine” is above 90%, then the study can be continued for this area.

α at 355 nm and β at 355 nm retrieved by the standard correction algorithm (SCA) from Aeolus Level 2A product are used in this study, as the SCA processing is capable to produce more stable α and β than the Mie channel algorithm

(Flament et al., 2021). Furthermore, the mid-bin product (sca_optical_properties_mid_bins) of the SCA product are chosen as a result from that the product retrieved as the mid-bin algorithm is more robust (Baars et al., 2021; Flament et al., 2021). To ensure a high data quality and hence to acquire the relationship between the optical properties and wind speed, a rigorous quality control has to be applied. In the aspect of quality control, negative α and β are excluded, and then the quality flags ("bin_1_clear" and "processing_qc_flag") provided in the Level 2A product are applied to filter out invalid data (Trapon et al., 2022). Additionally, the outliers are labeled and eliminated by the boxplot analysis. By using the lower quartiles Q_L (25% positions of the data) and upper quartiles Q_U (75% positions of the data), this method classifies the data below $Q_L - 3 \cdot (Q_U - Q_L)$ or above $Q_L + 3 \cdot (Q_U - Q_L)$ as outliers (Hoaglin et al., 1986). The Aeolus products do not differentiate between aerosol and layers, which means that the particle optical properties of a single data bin may contain a mixture of both types of information. Aeolus measured particulate β, combined with relative humidity (RH) and molecular β from the ECMWF NWP model provided in the Level 2A product are utilized to screen the cloud layers. It is considered that a cloud is quite likely to exist if the backscatter ratio (BR) (total backscatter coefficient/molecular backscatter coefficient) at 355 nm is larger than 2.5 or the RH is larger than 94% (Flamant et al., 2020). Therefore, in this study, when the BR is larger than 2.5 or the RH is higher than 94%, the corresponding data bin is regarded as cloud contaminated and is eliminated. With this cloud screening approach, in this study, 9%, 35%, 40% data in the altitude range of 0-2 km was eliminated for the NP area, the SP area and the SI area, respectively. Due to the instrument design of ALADIN, it can only detect the co-polar backscatter light, leading to the lack of the depolarized portion of the β (Flamant et al., 2020). According to Groß et al. (2015), the depolarization ratio at 355 nm of marine aerosol ($\delta_{mar,355nm}$) is approximately 0.02 when the RH is larger than 50%. Nevertheless, dried marine aerosol layers can significantly depolarize and the depolarization ratio will vary from 0.02 to around 0.1, so the typical $\delta_{mar,355nm}$ of humid marine aerosol (RH>50%) is not suitable for dried aerosol (Haarig et al. 2017; Bohlmann et al. 2018). Consequently, to correct the marine aerosol backscatter coefficient with the typical $\delta_{mar,355nm}$ of humid marine aerosol, the data with RH>50% is retained (around 95% data is retained), and thus with the typical $\delta_{mar,355nm}$ the total marine aerosol backscatter coefficient β_{mar} can be calculated by the following Eq. (1):

$$\beta_{mar} = (1 + \delta_{mar,355nm}) \cdot \beta_{mar,Aeolus-co}, \quad (1)$$

where $\beta_{mar,Aeolus-co}$ is the original marine aerosol backscatter coefficient measured by ALADIN. It should be illustrated that all the aerosol β s from Aeolus identified as $\beta_{mar,Aeolus-co}$ s and then utilized to calculate β_{mar} s by formula (1) is under the ideal assumption that marine aerosol is the only aerosol type in the study areas. Though the study areas are all located in the remote ocean far away from land and are evaluated as "marine aerosol dominate" by CALIOP, there are a few terrestrial aerosols like dust, polluted dust, polluted continental and smoke, with the total proportion of no more than 10% (see Section 4.1 for the detail). For the part of terrestrial aerosols, the depolarization ratios at 355 nm of them are 0.22-0.24 for dust, 0.16 for polluted dust, 0.01 for polluted continental and 0.03 for smoke, among which the dust's and the polluted dust's are much

larger than $\delta_{mar,355nm}$ (Floutsi et al., 2023). Consequently, regarding all the aerosols as marine aerosol and correcting β_{mar} by formula (1) leads to the obvious underestimation of the β for dust and polluted dust. Nevertheless, in view of the small proportions of dust (no more than 3.15%) and polluted dust (no more than 0.79%) above the study areas and thanks to the statistical analyses of data for a long term, the assumption that regarding all the aerosols as marine aerosol is considered not to critically impact the β_{mar} - wind speed relationship, while it should be noticed that the actual β is a little bit larger than the β_{mar}.

As for the wind vector data, Aeolus Level 2C product provides the u component (zonal components of wind vector) and v component (meridional components of wind vector) from the ECMWF model after assimilation of Level 2B observational wind product, at the same data bins of the Level 2A optical properties product. Hence the wind speed ws can be calculated with these two components by the following Eq. (2):

$$ws = \sqrt{u^2 + v^2} . \quad (2)$$

With the re-processed marine aerosol optical properties extinction coefficient α_{mar} and β_{mar}, and the corresponding ws, it is possible to explore the relationship between these parameters. At the beginning of data analyses, α_{mar}, β_{mar} and ws within the altitude range of 0 km to 2 km are selected, where the marine aerosol dominates according to the analysis of CALIOP VFM. Further, the whole study height range is divided into two individual layers. Referring the results of Luo et al. (2014), Luo et al. (2016) and Alexander et al. (2019), the MABL height of the remote ocean is summarized as around 1 km. Moreover, calculated with ECMWF provided boundary layer heights at the three study areas for the time period of 20 April 2020 to 26 May 2021, the mean values and the standard deviations are 787.47 ± 231.77 m at the NP area, 939.39 ± 360.20 m at the SP area and 1005.29 ± 366.60 m at the SI area. Hence, the boundary height of the two vertical layers is set as 1 km, approximately corresponding to the mean MABL height of remote ocean. Though the MABL heights are variable and thus set as 1 km will lead to the potential inaccuracies, restricted by the relatively low height resolution of Aeolus (0.25 km below 0.5 km, 0.5 km in the range of 0.5 km to 2 km), utilizing more precise height boundaries won't make more sense. It is considered that the statistical results of the 0-1 km layers and the 1-2 km layers are capable to generally represent the atmospheric conditions within the MABL and above the MABL. The lower layer with the altitude range of 0 km to 1 km is called Layer_L in this paper and the higher layer with the altitude range of 1 km to 2 km is called Layer_H. It is important to note that the lowest altitude bins of Aeolus observation products may contain the reflections from the surface or even be subsurface, thus they are contaminated and not representative of the atmospheric wind speed and the aerosol optical properties (Wu et al., 2022). Regarding the ocean applications of spaceborne lidars observations, it is known that the lidar attenuated backscatter coefficients of the bin containing the ocean surface can be affected by the processes at the surface of ocean, namely, stronger winds resulting in weaker backscattering (Josset et al., 2008). Labzovskii et al. (2023) indicated that Aeolus return signals are unlikely sensitive to ocean surface dynamical conditions (related to wind), which makes the analysis of marine aerosol optical properties in the MABL free from adverse effects stemming from ocean surface.

Nevertheless, during the data processing, it was discovered that all data (Level 2A particle optical properties, Level 2C wind vectors) below 0.25 km, which could be contaminated by reflections from the land or ocean surface, were all screened out using Aeolus quality control flags, then the lowest data bins became at around 0.25 km. This may indicate that the actual altitude range of marine aerosol optical properties in $\mathrm{Layer_L}$ is around 0.25 km to 1 km. Although the data near the sea-air interface are missing, all available data avoids the contamination of the ground return signals and eliminates the risk of being affected by ocean surface dynamical conditions. Over the selected ocean areas, the spatial distribution of the α_{mar}, β_{mar} and ws are acquired with the longitude-latitude grid of $5^{\circ} \times 5^{\circ}$ at two separate layers. Then the relationship analyses between the optical properties (α_{mar}, β_{mar}) and ws of these two layers are conducted by the average calculations of the optical properties along ws grids (1 $\mathrm{m \cdot s^{-1}}$) and the parametric curve fitting. For the average calculations, specifically, a grid with resolution of 1 $\mathrm{m \cdot s^{-1}}$ from 0 $\mathrm{m \cdot s^{-1}}$ to 30 $\mathrm{m \cdot s^{-1}}$ is defined and the mean values and the standard deviations are calculated along the grid at both layers above the study areas, respectively. It should be emphasized primarily that before the calculation of mean of each wind speed grid, the outliers larger/less than the mean plus/minus one standard deviation are eliminated. About 70% to 80% α_{mar} and β_{mar} are retained after the elimination. The quite strict outlier removal is conducted here to reject the data unrepresentative for marine aerosol (may be contaminated by cloud thus become higher than the typical range). Hence, it can guarantee the data quality and validity of the pure marine aerosol optical properties in the statistical analysis process. Moreover, the wind speed grid of which the data counts are less than 100 is considered unrepresentative and the statistical result of this grid is abandoned. The derived data of α_{mar}, β_{mar}, averaged $\mathrm{AOD_{mar}}$ and $\mathrm{LR_{mar}}$ are obtained and discussed, as well. The $\mathrm{AOD_{mar}}$ is acquired by integrating Aeolus retrieved α_{mar} within 2 km of every single profile. The $\mathrm{AOD_{mar}}$ is calculated within the height of 2 km in order to compare with the previous result of CALIOP, where the integration height is the same as that in this study. The averaged $\mathrm{AOD_{mar}}$ along the ws grid are obtained and then are compared with the $\mathrm{AOD_{mar}}$ - ws relationships from a previous study in Section 4.4.1. The $\mathrm{LR_{mar}}$ are derived via dividing α_{mar} by β_{mar} for each corresponding data bin. The spatial distribution of the $\mathrm{LR_{mar}}$ are presented in Section 4.2, meanwhile the relationship between the variations of the $\mathrm{LR_{mar}}$ along ws grids and the marine aerosol particle size are discussed in Section 4.4.2.

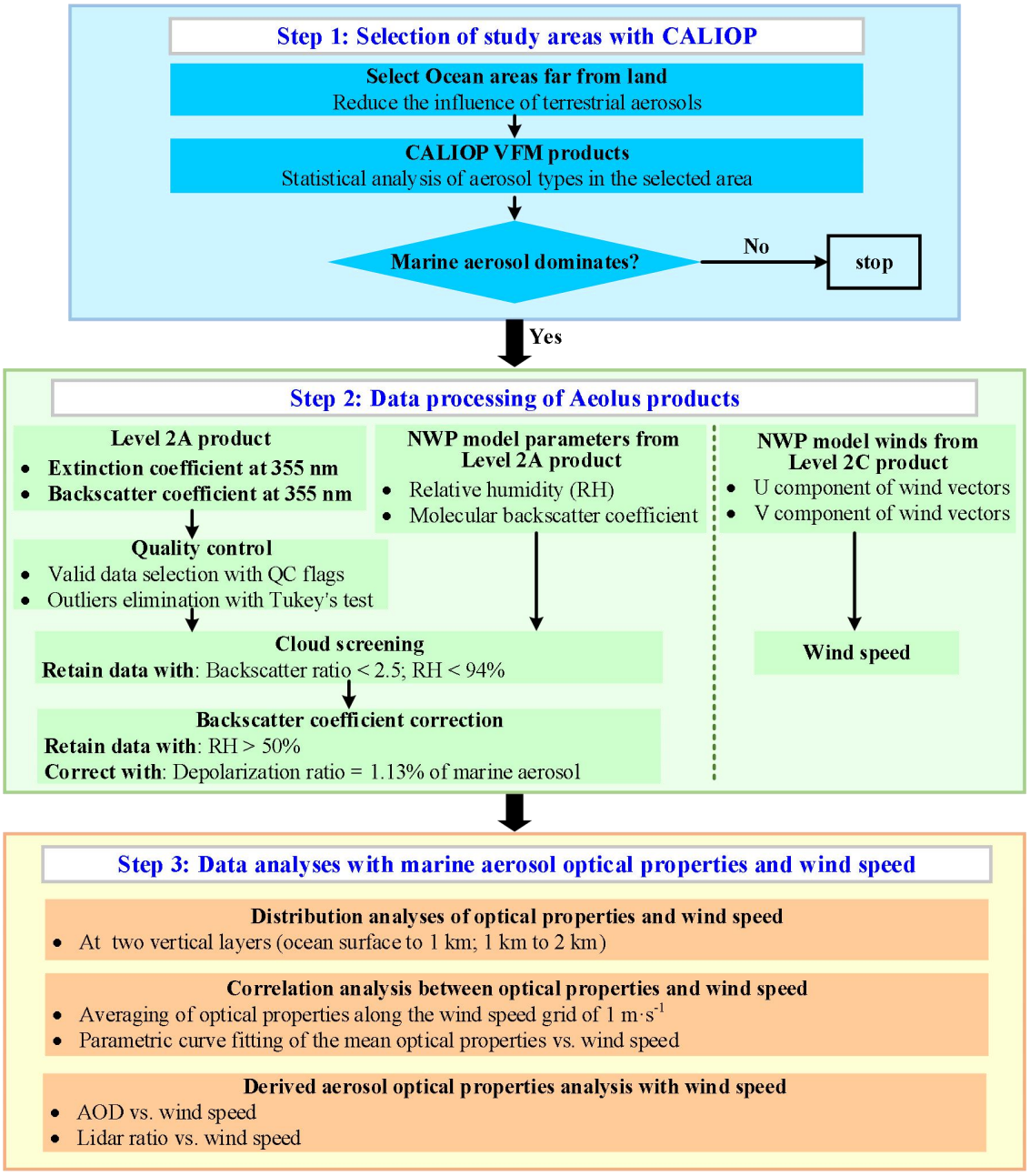

Figure 2: Flowchart of the study methodology.

4 Results and discussion

4.1 Aerosol types analysis

To verify the domination of marine aerosol, as introduced in Section 3 of this paper, the CALIOP VFM aerosol classification products are applied. The proportions of eight aerosol types (marine, dusty marine, dust, polluted dust, continental, polluted continental, smoke and others) are counted at two vertical layers defined in Section 3 over the NP area, the SP area and the SI area, respectively, as shown the histograms in Fig. 3. The proportions of marine aerosol at $Layer_L$ in these three separate areas are 87%, 84% and 84% while the proportions at $Layer_H$ are 84%, 79% and 79% respectively, which are all larger than 75%. Moreover, the percentage sums of marine aerosol and dusty marine aerosol are all above 90%, at both layers and over all study areas. Consequently, the selected areas NP, SP and SI can be regarded as the marine aerosol dominating areas. It should be illustrated that "dusty marine" was a new aerosol subtype raised for the first time in the version 4.10 of the CALIOP VFM product and was absent in the version 3.41, which was identified from part of version 3.41's "polluted dust" with the criteria of "surface type" and "layer base altitude". Using the version 3.41 of the CALIOP VFM data for the period of 19 January 2022 to 4 July 2022 led to the underestimate of "dusty marine" portion and the total marine aerosol portion. Even though under the condition of underestimate, the percentage of total marine aerosol are larger than 90%, which means the real proportion of total marine aerosol is higher, and hence the conclusion that the marine aerosol dominates in the altitude range of 0-2 km above these three areas is still valid.

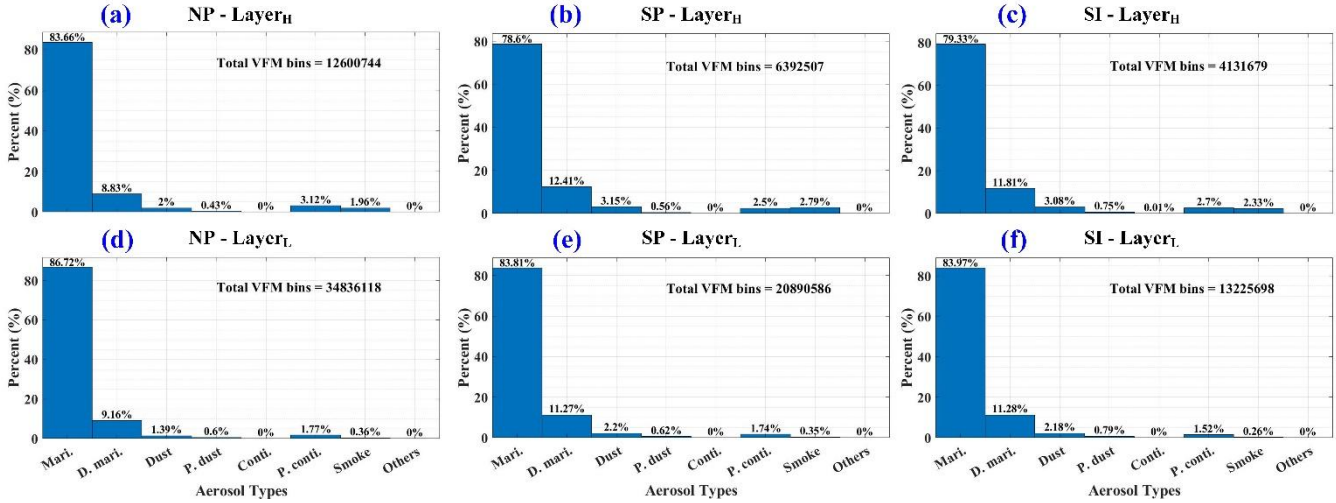

Figure 3: Aerosol types statistical analyses over (a)(d) the NP area, (b)(e) the SP area and (c)(f) the SI area at two sperate layers.

In this section, the study areas in this paper are introduced. With the aerosol types statistical analyses, the dominations of marine aerosol are confirmed over these three areas. It should be illustrated that among the areas, the NP area is mainly located in low latitudes or tropics, while the SP area and the SI area are in mid-latitude region.

4.2 Spatial distribution of wind speed and aerosol optical properties

With Aeolus L2A products (particle optical properties) and L2C products (ECMWF model winds) from April 2020 to July 2022, calculated for every $5^{\circ} \times 5^{\circ}$ grid, the averaged ws, α_{mar}, β_{mar} and $\mathrm{LR}_{\mathrm{mar}}$ spatial distributions of $\mathrm{Layer}_{\mathrm{H}}$ and $\mathrm{Layer}_{\mathrm{L}}$ are acquired. The averaged atmospheric parameters spatial distributions of the NP area, the SP area and the SI area are presented in Fig. 4, Fig. 5 and Fig. 6, respectively. These figures describe the atmospheric background state of optical properties and wind speed within ($\mathrm{Layer}_{\mathrm{L}}$) and above ($\mathrm{Layer}_{\mathrm{H}}$) the MABL over the study areas. Additionally, the mean values and the standard deviations of these atmospheric parameters at $\mathrm{Layer}_{\mathrm{H}}$ and $\mathrm{Layer}_{\mathrm{L}}$ are calculated for each study area by averaging the spatial distributions of $5^{\circ} \times 5^{\circ}$ grid, and are presented in Fig. 7.

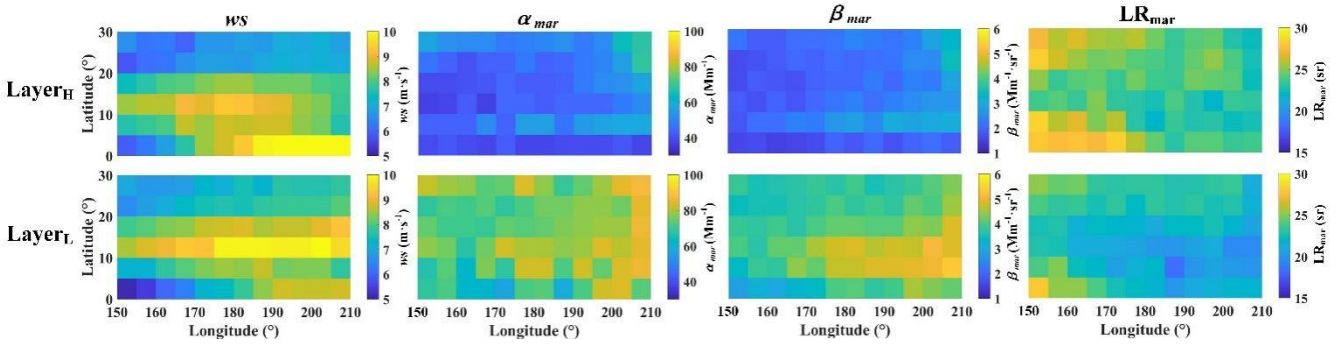

Figure 4: Wind speed (ws), marine aerosol extinction coefficient (α_{mar}), marine aerosol backscatter coefficient (β_{mar}), and marine aerosol lidar ratio ($\mathrm{LR}_{\mathrm{mar}}$) spatial distributions above the North Pacific (NP) area at $\mathrm{Layer}_{\mathrm{H}}$ and $\mathrm{Layer}_{\mathrm{L}}$.

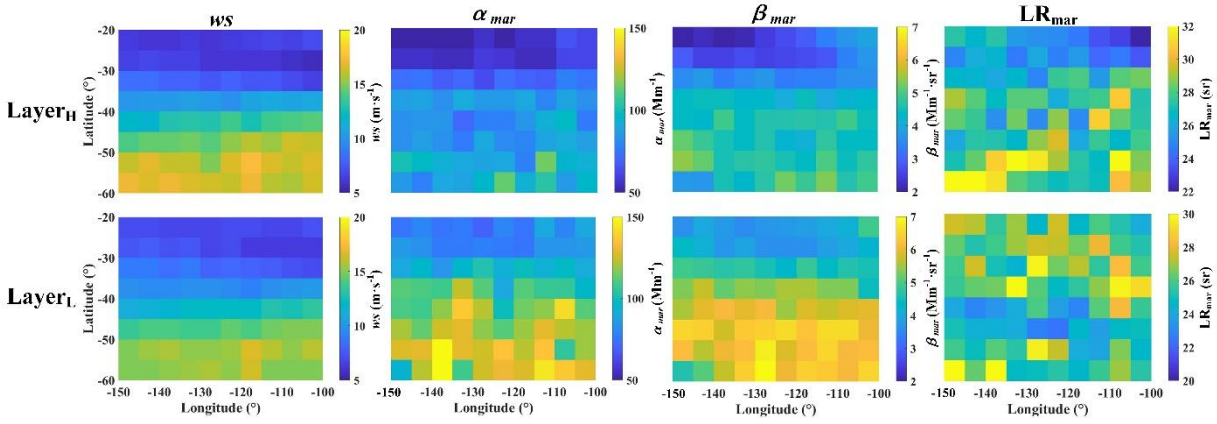

Figure 5: Wind speed (ws), marine aerosol extinction coefficient (α_{mar}), marine aerosol backscatter coefficient (β_{mar}), and marine aerosol lidar ratio ($\mathrm{LR}_{\mathrm{mar}}$) spatial distributions above the South Pacific (SP) area at $\mathrm{Layer}_{\mathrm{H}}$ and $\mathrm{Layer}_{\mathrm{L}}$.

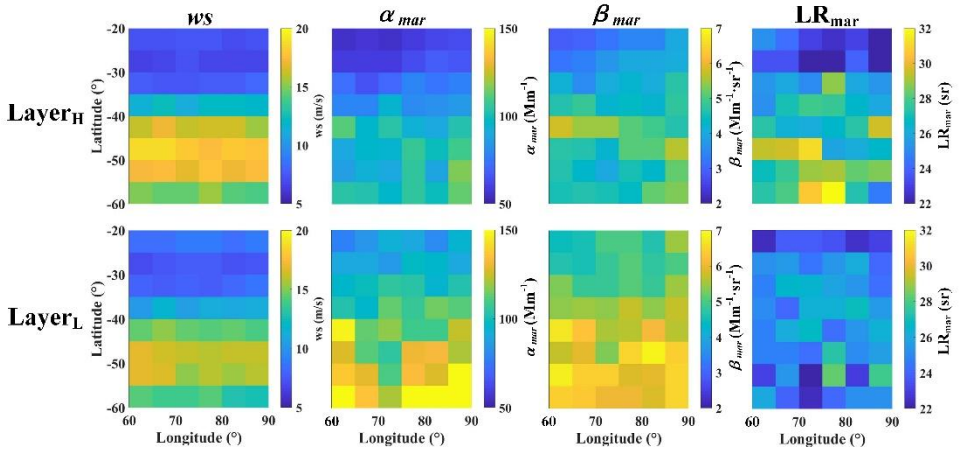

Figure 6: Wind speed (ws), marine aerosol extinction coefficient (α_{mar}), marine aerosol backscatter coefficient (β_{mar}), and lidar ratio ($\mathrm{LR_{mar}}$) spatial distributions above the South Indian (SI) area at $\mathrm{Layer_H}$ and $\mathrm{Layer_L}$.

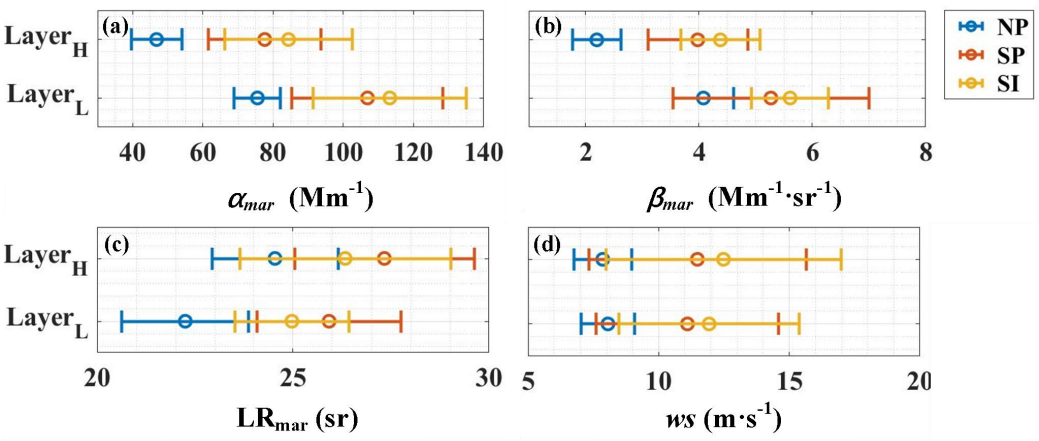

315 **Figure 7: Mean values at $\mathrm{Layer_H}$ and $\mathrm{Layer_L}$ of (a) marine aerosol extinction coefficient (α_{mar}), (b) marine aerosol backscatter coefficient (β_{mar}), (c) marine aerosol lidar ratio ($\mathrm{LR_{mar}}$) and (d) wind speed (ws) above the North Pacific (NP) area (blue standard deviation bars), the South Pacific (SP) area (red standard deviation bars), and the South Indian (SI) area (yellow standard deviation bars).**

In Fig. 7, the mean values and the standard deviations of the parameters represent the background atmospheric states within
320 the MABL ($\mathrm{Layer_L}$) and over the MABL ($\mathrm{Layer_H}$) above each study areas. The averaged ws are $8.1\pm1.0\ \mathrm{m\cdot s^{-1}}$, $11.1\pm3.5\ \mathrm{m\cdot s^{-1}}$, $12.0\pm3.5\ \mathrm{m\cdot s^{-1}}$ at $\mathrm{Layer_L}$, while $7.9\pm1.1\ \mathrm{m\cdot s^{-1}}$, $11.5\pm4.2\ \mathrm{m\cdot s^{-1}}$, $12.5\pm4.5\ \mathrm{m\cdot s^{-1}}$ at $\mathrm{Layer_H}$, above the NP area, the SP area, and the SI area, respectively. The averaged α_{mar} are $76\pm7\ \mathrm{Mm^{-1}}$, $107\pm22\ \mathrm{Mm^{-1}}$, $113\pm22\ \mathrm{Mm^{-1}}$ at $\mathrm{Layer_L}$, while $47\pm7\ \mathrm{Mm^{-1}}$, $78\pm16\ \mathrm{Mm^{-1}}$, $84\pm18\ \mathrm{Mm^{-1}}$ at $\mathrm{Layer_H}$, above the NP area, the SP area, and the SI area, respectively. The averaged β_{mar} are $4.1\pm0.5\ \mathrm{Mm^{-1}\cdot sr^{-1}}$, $5.3\pm1.7\ \mathrm{Mm^{-1}\cdot sr^{-1}}$, $5.6\pm0.7\ \mathrm{Mm^{-1}\cdot sr^{-1}}$ at $\mathrm{Layer_L}$, while

2.2 ± 0.4 $Mm^{-1} \cdot sr^{-1}$, 4.0 ± 0.9 $Mm^{-1} \cdot sr^{-1}$, 4.4 ± 0.7 $Mm^{-1} \cdot sr^{-1}$ at $Layer_H$, above the NP area, the SP area, and the SI area, respectively. The averaged LR_{mar} are 22.3 ± 1.6 sr, 25.9 ± 1.8 sr, 25.0 ± 1.5 sr at $Layer_L$, while 24.5 ± 1.6 sr, 27.3 ± 2.3 sr, 26.3 ± 2.7 sr at $Layer_H$, above the NP area, the SP area, and the SI area, respectively. It is reported that the typical ranges of α_{mar} and β_{mar} at 532 nm over remote ocean areas are around 60 Mm^{-1} to 80 Mm^{-1} and around 1 $Mm^{-1} \cdot sr^{-1}$ to 5 $Mm^{-1} \cdot sr^{-1}$, respectively, observed and retrieved by CALIOP (Prijith et al., 2014; Kiliyanpilakkil and Meskhidze, 2011). Applying the typical α_{mar} Ångström exponent from 532 nm to 355 nm of 0.7 ± 1.3 and the typical β_{mar} Ångström exponent from 532 nm to 355 nm of 0.8 ± 0.1 (Floutsi et al., 2023), the converted typical ranges of α_{mar} and β_{mar} at 355 nm can be calculated, which are around 47 Mm^{-1} to 180 Mm^{-1} and around 1.3 $Mm^{-1} \cdot sr^{-1}$ to 7.2 $Mm^{-1} \cdot sr^{-1}$. Compared with the typical ranges of α_{mar} and β_{mar} at 355 nm, calculated from CALIOP retrieved typical ranges of marine aerosol optical properties and the typical conversion coefficients, it is considered that the Aeolus retrieved α_{mar} and β_{mar} are reasonable. The mean values of ws, α_{mar} and β_{mar} above the NP area are the lowest among the three areas, both at $Layer_H$ and $Layer_L$, which may be because that this area is located in low latitudes region of the Northern Hemisphere. The highest mean wind speed of the SI area corresponds to the highest α_{mar} and β_{mar}. The mean wind speeds of $Layer_H$ are both larger than those of $Layer_L$ in the SP area and in the SI area, while the phenomenon is on the contrary in the NP area. It is worth noting that in all the study areas, the averaged α_{mar} and β_{mar} at $Layer_L$ are larger than those at $Layer_H$, illustrating that the majority of the aerosol from ocean is trapped in the MABL while a fraction of marine aerosol can be elevated above the MABL. In the aspect of mean LR_{mar}, the values at $Layer_H$ are all higher than at $Layer_L$, and all the values are in a reasonable range referring to Bohlmann et al. (2018), Groß et al. (2011), Groß et al. (2015) and Floutsi et al. (2023).

Figure 4, Fig. 5, and Fig. 6 presents the parameters distributions at two layers above the NP area, the SP area and the SI aera. Primarily, the spatial variations of ws, α_{mar}, β_{mar} are more apparent along the meridian than zonally, both at $Layer_H$ and at $Layer_L$. In the aspect of $Layer_L$, there are separate distinct high wind speed regions or belts along latitude in the three areas, which are 5 ° N to 20 ° N region of the NP area with the wind speed bins of approximately 8 $m \cdot s^{-1}$ to more than 10 $m \cdot s^{-1}$, 40 ° S to 60 ° S region of the SP area with the wind speed bins of more than 10 $m \cdot s^{-1}$ to approximately 17 $m \cdot s^{-1}$, and 35 ° S to 60 ° S region of the SI area with the wind speed bins of more than 10 $m \cdot s^{-1}$ to approximately 17 $m \cdot s^{-1}$ as well. Inspection of marine aerosol optical properties, α_{mar} and β_{mar} in the high wind speed regions are obviously larger than in other regions. Hence, it can be inferred that, in the MABL, the wind speed and the marine aerosol optical properties tend to be positively correlated. Referring to $Layer_H$, shown in the upper four panels of Fig. 4, Fig. 5 and Fig. 6, it can be found that the spatial variation trends of ws, α_{mar}, β_{mar} in the three areas are alike with those at $Layer_L$. The evident high wind speed regions, where the wind speeds are up to around 8-10 $m \cdot s^{-1}$ in 5 ° N to 20 ° N of the NP area, 15-18 $m \cdot s^{-1}$ in 40 ° S to 60 ° S

of the SP area and 13-19 $\mathrm{m \cdot s^{-1}}$ in 35 ° S to 60 ° of the SI area, also exist at $\mathrm{Layer_H}$ while α_{mar} and β_{mar} are slightly enhanced in these regions, which indicates that the wind speed may still have weak positive influence on the marine aerosol optical properties at the higher atmosphere layer above the MABL. Some spatial distribution differences of ws, α_{mar}, β_{mar} between the three areas can be discovered as well. As for the SP area and the SI area, ws, α_{mar}, β_{mar} all mainly present increasing tendencies from north to south. In term of the NP area, besides the obvious enhancements of ws, α_{mar}, β_{mar} in the high wind speed belt, the gradual enhancements of these atmospheric parameters are presented from west to east in this area.

At both layers of the NP area and at $\mathrm{Layer_L}$ of the SP area, the $\mathrm{LR_{mar}}$ turn out lower in the relatively high wind speed regions, which illustrates a possible negative correlation between $\mathrm{LR_{mar}}$ and wind speed. The relationship between these two parameters is analysed and discussed in detail in Section 4.4.2 of this paper.

To conclude, this section presents the atmospheric background state of optical properties and wind speed, and analyses the spatial distributions of ws, α_{mar}, β_{mar} jointly at $\mathrm{Layer_H}$ and $\mathrm{Layer_L}$ above the NP area, the SP area and the SI area, respectively. The α_{mar}, β_{mar} retrieved from Aeolus Level 2A products are in reasonable agreement with CALIOP and the Aeolus-derived $\mathrm{LR_{mar}}$ are also reasonable. It is found that, both at $\mathrm{Layer_H}$ and at $\mathrm{Layer_L}$, spatially, the wind speed and α_{mar}, β_{mar} show positive correlation though the optical properties at $\mathrm{Layer_L}$ are greater than those at $\mathrm{Layer_H}$, indicating that both layers receive the input of the aerosol produced from ocean by the wind but the majority of the marine aerosol are trapped in the MABL while only a small fraction can be elevated into the higher layer. In addition, as the three study areas are located in different regions, the spatial distributions of ws, α_{mar}, β_{mar} are different.

4.3 Relationship between marine aerosol optical properties and wind speed

In order to determine the relationship between marine aerosol optical properties and corresponding wind speed, utilizing the method introduced in Section 3, the mean values and standard deviations (after the outlier removal) of α_{mar} and β_{mar} along with wind speed grid at two layers above the NP area, the SP area and the SI area are shown in the panel (a) and (b) of Fig. 8, Fig. 9, and Fig. 10, respectively. The regression curves of the optical properties are presented in those figures as well. Power law function is utilized for the curve fitting to describe the trend of marine aerosol optical properties with wind speed. Besides, the data counts in every wind speed grid are shown as the histograms in the panel (a) and (b) of Fig. 8, Fig. 9, and Fig. 10. In order to illustrate the variation tendencies α_{mar} and β_{mar}, the slopes of α_{mar} and β_{mar} with wind speed are also provided in the panel (c) and (d) of Fig. 8, Fig. 9, and Fig. 10. Table 1 summarizes the regression functions together with the corresponding R^2, and the proportions of different wind speed bins together with the count sums, grouped by areas, layers and optical properties.

From the statistical results with wind speed grids and wind speed ranges, it can be found that most of the wind speeds are below 15 $m \cdot s^{-1}$ above the NP area, both at $Layer_H$ and $Layer_L$, meanwhile the proportion of low wind speed ($0< ws \leqslant 8$) is slightly higher at $Layer_H$ than at $Layer_L$. As for the SP area and the SI area, the high wind speed ($ws >15$) accounts for around one fifth and a quarter respectively, and the low wind speed proportion over the SP area is higher than that over the SI area. The wind speed distribution is more concentrated at $Layer_L$ than at $Layer_H$ above these two areas, in view of the lower proportion of low/high wind speed and the higher proportion of middle wind speed ($8< ws \leqslant 15$) at $Layer_L$.

Table 1: Regression functions of the averaged optical properties and the wind speed grids, together with the corresponding wind speed distributions, grouped by areas and layers.

Area	Layer	Optical property	Regression function	R^2	Proportion of wind speed bins ($m \cdot s^{-1}$)			Number of counts
					$0< ws \leqslant 8$	$8< ws \leqslant 15$	$ws >15$	
NP	H	α_{mar}	$\alpha_{mar} = 0.084 \cdot ws^{1.8} + 42$	0.95	0.53	0.46	0.01	55758
		β_{mar}	$\beta_{mar} = 0.050 \cdot ws^{1.3} + 1.4$	0.97	0.54	0.45	0.01	64191
	L	α_{mar}	$\alpha_{mar} = 0.070 \cdot ws^{2.3} + 64$	0.99	0.49	0.50	0.01	44857
		β_{mar}	$\beta_{mar} = 0.15 \cdot ws^{1.2} + 2.1$	0.99	0.51	0.48	0.01	55117
SP	H	α_{mar}	$\alpha_{mar} = 5.0 \cdot ws^{0.84} + 54$	0.95	0.46	0.34	0.20	34088
		β_{mar}	$\beta_{mar} = 1.3 \cdot ws^{0.48} + 1.1$	0.96	0.49	0.31	0.20	30348
	L	α_{mar}	$\alpha_{mar} = 6.1 \cdot ws^{0.83} + 73$	0.98	0.45	0.38	0.17	25783
		β_{mar}	$\beta_{mar} = 1.8 \cdot ws^{0.47} + 1.1$	0.97	0.47	0.36	0.17	23854
SI	H	α_{mar}	$\alpha_{mar} = 0.65 \cdot ws^{1.4} + 56$	0.95	0.40	0.35	0.25	19552
		β_{mar}	$\beta_{mar} = 0.60 \cdot ws^{0.59} + 1.7$	0.96	0.42	0.33	0.25	16473
	L	α_{mar}	$\alpha_{mar} = 1.1 \cdot ws^{1.2} + 81$	0.92	0.38	0.41	0.21	15953
		β_{mar}	$\beta_{mar} = 1.2 \cdot ws^{0.47} + 1.7$	0.97	0.46	0.36	0.18	13923

Generally, in all cases shown in Fig. 8, Fig. 9 and Fig. 10, the optical properties at $Layer_L$ are all larger than those at $Layer_H$ in the same wind speed grid, while the variations of marine aerosol optical properties along with wind speed grid can be clearly observed that the tendency is increasing with the wind speed. Moreover, the regression curves are fitted pretty well as the R^2 are all above 0.90.

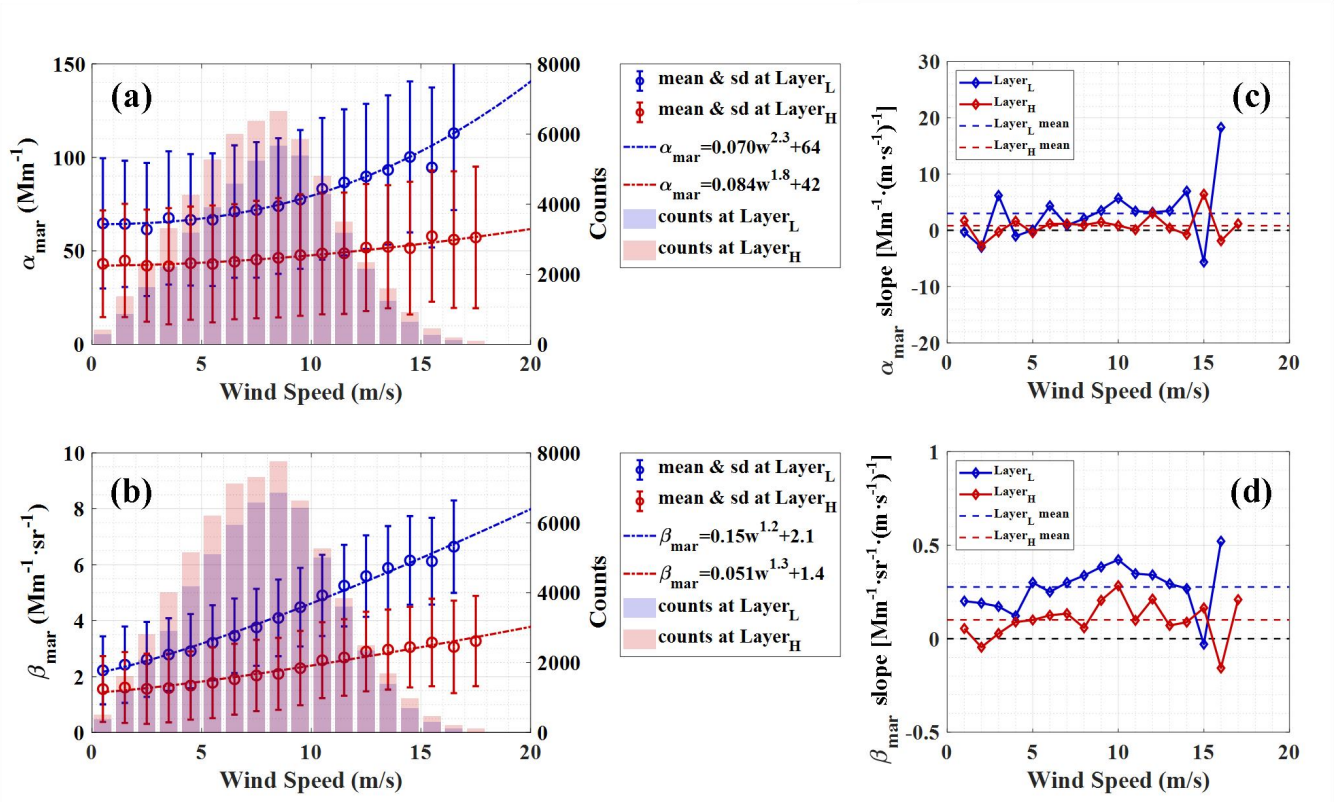

Figure 8: Relationship between marine aerosol optical properties ((a) for α_{mar}, (b) for β_{mar}) and wind speed above the NP area. The blue circles and error bars represent the means and standard deviations of the optical properties along wind speed grids at $\mathrm{Layer_L}$, while the reds represent the same items at $\mathrm{Layer_H}$. The blue and red dotted-dashed lines are the optical property averages regression curves fitted along the wind speed grid at $\mathrm{Layer_L}$ and $\mathrm{Layer_H}$, respectively. The blue and red histograms indicate the data counts of every wind speed grid at $\mathrm{Layer_L}$ and $\mathrm{Layer_H}$, respectively. (c) and (d) represent the slopes of α_{mar} and β_{mar} with wind speed at $\mathrm{Layer_L}$ (blue lines) and $\mathrm{Layer_H}$ (red lines), respectively, while the blue dashed lines and the red dashed lines show the mean values of the slopes at two layers.

It can be found from the panel (a) and (b) of Fig. 8, in the NP area, α_{mar} at $\mathrm{Layer_L}$ increases from 64 $\mathrm{Mm^{-1}}$ at 0-1 $\mathrm{m\cdot s^{-1}}$ wind speed interval to 113 $\mathrm{Mm^{-1}}$ at 16-17 $\mathrm{m\cdot s^{-1}}$ wind speed interval, while it at $\mathrm{Layer_H}$ increases from 42 $\mathrm{Mm^{-1}}$ at 0-1 $\mathrm{m\cdot s^{-1}}$ wind speed interval to 57 $\mathrm{Mm^{-1}}$ at 17-18 $\mathrm{m\cdot s^{-1}}$ wind speed interval; β_{mar} at $\mathrm{Layer_L}$ increases from 2.2 $\mathrm{Mm^{-1}\cdot sr^{-1}}$ at 0-1 $\mathrm{m\cdot s^{-1}}$ wind speed interval to 6.6 $\mathrm{Mm^{-1}\cdot sr^{-1}}$ at 16-17 $\mathrm{m\cdot s^{-1}}$ wind speed interval, while it at $\mathrm{Layer_H}$ increases from 1.6 $\mathrm{Mm^{-1}\cdot sr^{-1}}$ at 0-1 $\mathrm{m\cdot s^{-1}}$ wind speed interval to 3.3 $\mathrm{Mm^{-1}\cdot sr^{-1}}$ at 17-18 $\mathrm{m\cdot s^{-1}}$ wind speed interval. The increments of these two parameters at $\mathrm{Layer_L}$ are much larger than at $\mathrm{Layer_H}$. Moreover, the exponents of the regression functions are all larger than 1, indicating the growth rates of the optical properties along the wind grid increases. Referring to the panel (c) and (d) of Fig. 8, the slopes' mean values of the α_{mar} and β_{mar} at $\mathrm{Layer_L}$ are higher than those at $\mathrm{Layer_H}$. Besides, the

slopes at Layer_L are mostly larger than that at Layer_H within the same wind speed interval, i.e., the optical properties at Layer_L will increase more rapidly with wind speed. It is worth noticing that for the case where the wind speed is above 10 $\text{m}\cdot\text{s}^{-1}$, the slopes of β_{mar} show decreasing tendencies, whereas for the condition where the wind speed is lower than 10 $\text{m}\cdot\text{s}^{-1}$, the values of β_{mar} slopes present increasing tendencies, indicating the better fitting by power law functions at lower
415 wind speed. This phenomenon may imply that there might be two distinct variation trends of β_{mar} above or below the wind speed of 10 $\text{m}\cdot\text{s}^{-1}$.

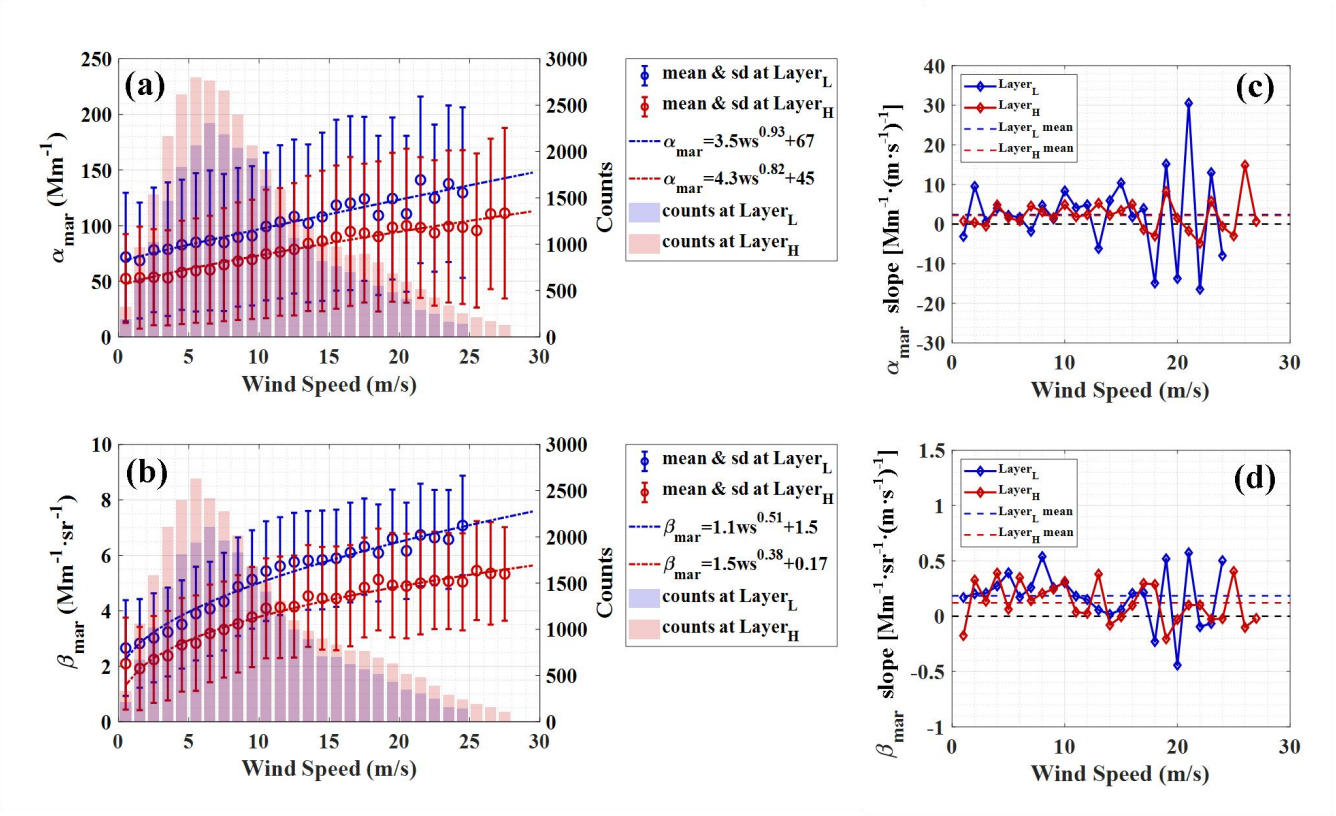

Figure 9: Relationship between marine aerosol optical properties and wind speed above the SP area. The items represent the same as those of Fig. 8.

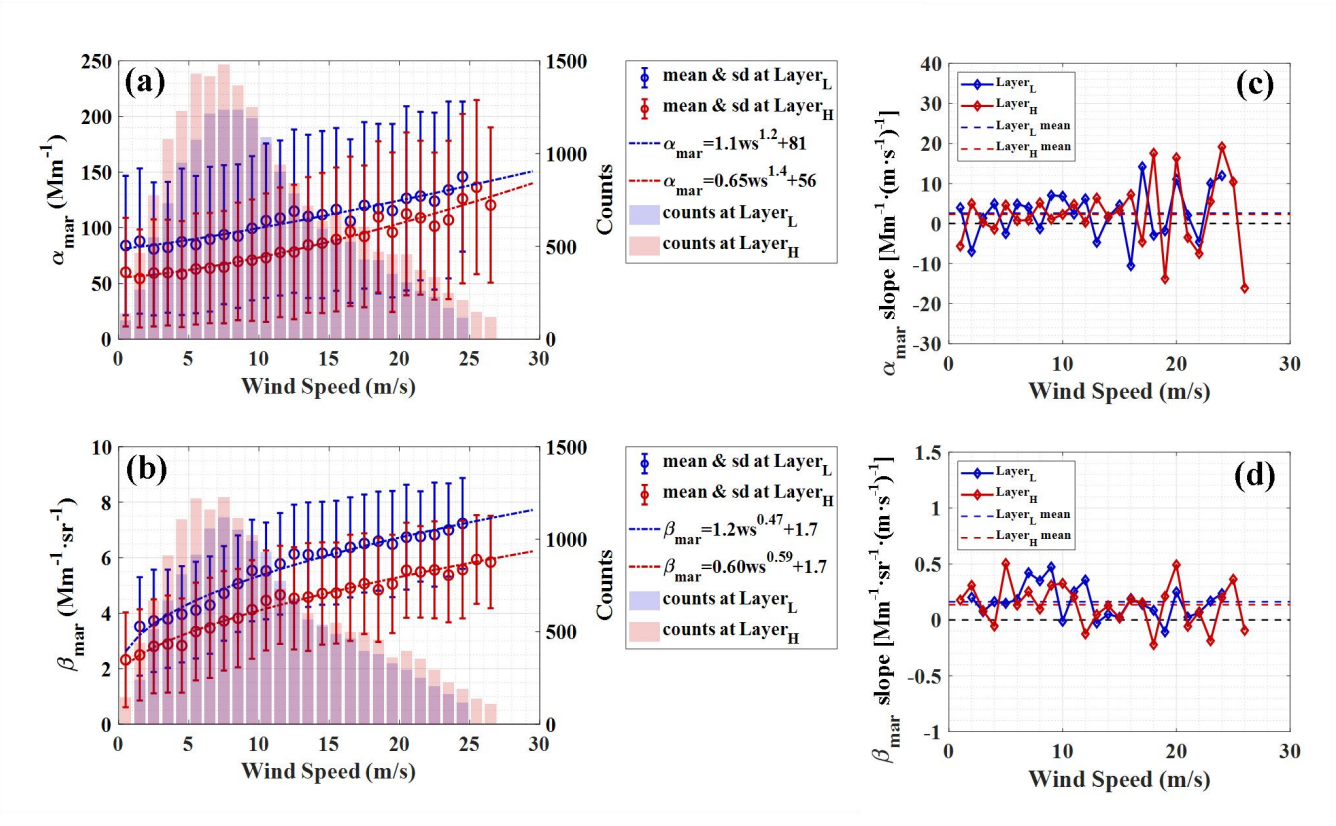

Figure 10: Relationship between marine aerosol optical properties and wind speed above the SI area. The items represent the same as those of Fig. 8.

For the SP area and the SI area, the maximal wind speed can reach up to 28 $\mathrm{m\cdot s^{-1}}$, while the variations of the optical properties along with wind speed are more complicated. In Fig. 9 (a), the α_{mar} over the SP area show approximate linear growth tendencies with wind speed both at $\mathrm{Layer_L}$ and at $\mathrm{Layer_H}$, with the fitting functions' exponents of 0.93 and 0.82. The α_{mar} increase from 72 $\mathrm{Mm^{-1}}$ and 52 $\mathrm{Mm^{-1}}$ to 130 $\mathrm{Mm^{-1}}$ and 111 $\mathrm{Mm^{-1}}$ for $\mathrm{Layer_L}$ and $\mathrm{Layer_H}$, respectively. Figure 9 (b) shows that the β_{mar} above the SP area increase from 2.7 $\mathrm{Mm^{-1}\cdot sr^{-1}}$ and 2.1 $\mathrm{Mm^{-1}\cdot sr^{-1}}$ to 7.0 $\mathrm{Mm^{-1}\cdot sr^{-1}}$ and 5.3 $\mathrm{Mm^{-1}\cdot sr^{-1}}$, with the fitting functions' exponents of 0.51 and 0.38 for $\mathrm{Layer_L}$ and $\mathrm{Layer_H}$. From Fig. 10 (a) and (b), it can be found that the variations of α_{mar} and β_{mar} with wind speed in the SI area are similar to those in the SP area, except for that the fitting functions' exponents of β_{mar} are larger than 1, which are 1.2 and 1.4 for $\mathrm{Layer_L}$ and $\mathrm{Layer_H}$, respectively. In the $\mathrm{Layer_H}$ of SI area, α_{mar} at above 25 $\mathrm{m\cdot s^{-1}}$ can reach up to 137 $\mathrm{Mm^{-1}}$, much larger than that of around 110 $\mathrm{Mm^{-1}}$ in the SP area. The panel (c) and (d) of Fig. 9 and Fig. 10 show the slopes of α_{mar} and β_{mar} with the wind speed above the SP area and the SI area. In these four panels, the blue dashed lines (slopes' mean values at $\mathrm{Layer_L}$) are all higher than the red lines

(slopes' mean values at $Layer_H$), illustrating that the increments of α_{mar} and β_{mar} per unit wind speed at $Layer_L$ are larger than those at $Layer_H$, which implies that the input of marine aerosol driven by wind at $Layer_L$ is stronger than at $Layer_H$. Focusing on the panel (c) of Fig. 9 and Fig. 10, it can be seen that, for both layers of the SP area and the SI area, the slopes of α_{mar} below 15 $m \cdot s^{-1}$ are almost all larger than 0, fluctuating slightly around the mean values, while the slopes of α_{mar} above 15 $m \cdot s^{-1}$ fluctuate drastically. This phenomenon may indicate that below 15 $m \cdot s^{-1}$, both layers continually receive the input of marine aerosol driven by wind, nevertheless when the wind speed is higher than 15 $m \cdot s^{-1}$, the dependency of marine aerosol on wind become lower. As for the slopes of β_{mar} above the SP area and the SI area, from the panel (d) of Fig. 9 and Fig. 10, it can be found obviously that for both layers, the slopes of β_{mar} decrease above around 10 $m \cdot s^{-1}$. The corresponding variations of β_{mar} above the SP area and the SI area are shown in the panel (b) of Fig. 9 and Fig. 10, of which the β_{mar} increase with higher slopes at the wind speed range of 0-10 $m \cdot s^{-1}$ while the slopes of the increasing become lower when the wind speed is above 10 $m \cdot s^{-1}$. This phenomenon might indicate that the increasing of β_{mar} with wind speed includes two separate trends regarding 10 $m \cdot s^{-1}$ as the change point, consist with the surmise raised in the analysis of the NP area. We named these two wind speed (15 $m \cdot s^{-1}$ for α_{mar}, 10 $m \cdot s^{-1}$ for β_{mar}) "slope variation point" in this paper. Table 2 presents the averaged slopes (Mean) and the corresponding standard deviations (SD) of α_{mar} and β_{mar} below and above the slope variation point, for the two layers of the SP and SI areas. All of the averaged slopes below the slope variation points are larger than those above the slope variation points, except for the α_{mar} in the SI area. The reason for the inverse results of α_{mar} in the SI area may be due to its rapid increase above 24 $m \cdot s^{-1}$. All of the SDs of β_{mar} above the slope variation points are greater than those below, indicating a more fluctuating growth phase above the slope variation points. These results could provide the evidence for the statement that the wind-driven enhancement of marine aerosol includes two phases: one is a rapid growth phase with high dependency of wind, and another is a slower growth phase with higher fluctuations.

Table 2: Mean ± SD of the slopes below and above the slope variation point, grouped by areas and layers.

Optical property	Area	Layer	Mean ± SD of the slopes [$Mm^{-1} \cdot (m \cdot s^{-1})^{-1}$ for α_{mar}, $Mm^{-1} \cdot sr^{-1} \cdot (m \cdot s^{-1})^{-1}$ for β_{mar}]	
			Below slope variation point	Above slope variation point
α_{mar}	SP	H	2.48 ± 1.81	1.79 ± 5.71
		L	3.11 ± 4.62	1.26 ± 16.11
	SI	H	1.96 ± 3.10	2.81 ± 12.59
		L	2.16 ± 4.28	3.28 ± 8.79
β_{mar}	SP	H	0.20 ± 0.17	0.07 ± 0.17

		L	0.28 ± 0.11	0.12 ± 0.29
	SI	H	0.21 ± 0.16	0.09 ± 0.20
		L	0.22 ± 0.16	0.12 ± 0.13

Consequently, for all of the measurement cases, the marine aerosol optical properties at Layer_L are larger than those at Layer_H in any identical wind speed interval, indicating that the MABL possibly receive more marine aerosol produced and transport from the sea-air interface, while the higher layer above the MABL with the upper boundary of 2 km can also be influenced by the marine aerosol but less. The slopes' mean values of α_{mar} and β_{mar} at Layer_L are all larger than at Layer_H, which implies that the marine aerosol enhancements caused by the background wind are more intensive at the MABL. It should be noticed that the slopes change during α_{mar} and β_{mar} increasing with wind speed. The slope variation point of α_{mar} ($15\ \text{m}\cdot\text{s}^{-1}$) is greater than that of β_{mar} ($10\ \text{m}\cdot\text{s}^{-1}$), and above them the enhancement rate becomes lower. It might illustrate that the impact of wind on marine aerosol enhancement includes two phases, among them one is a rapid growth phase with high dependency of wind, and another is a slower growth phase with more fluctuations after the slope variation points.

4.4 Dependency of aerosol optical depth and lidar ratio with wind speed

4.4.1 Marine aerosol optical depth vs. wind speed

As introduced in Section 1 of this paper, almost all the previous researches on the relationship between marine aerosol's optical properties and wind speed focused on the AOD of marine aerosol. In this study, as well, the attempt on the averaged 0-2 km AOD_mar of individual wind speed grid calculation has been conducted to compare the AOD_mar - *ws* relationship from previous study. The AOD_mar of every single profile is acquired by integrating Aeolus retrieved α_{mar} within 2 km. The wind speed profiles are also averaged for 2 km to correspond to the AOD_mar data. Then the relationship between the AOD_mar and the wind speeds is obtained by averaging the AOD_mar in each wind speed interval ($0\ \text{m}\cdot\text{s}^{-1}$ - $30\ \text{m}\cdot\text{s}^{-1}$, stepped by $1\ \text{m}\cdot\text{s}^{-1}$). The AOD_mar - *ws* relationship is also explored utilizing the products from the A-Train satellites (Kiliyanpilakkil and Meskhidze, 2011). "clean marine" aerosol AOD at 532 nm above ocean surface (up to 2 km) provided by CALIOP and 10 m daily wind speed provided by AMSR-E were used. It should be noticed that the wind speed used in Kiliyanpilakkil and Meskhidze (2011) is daily ocean surface wind speed, different from that in this study, which is instantaneous layer-averaged wind speed. Collecting the data for the time period from 2006 to 2011 over 15 remote ocean regions globally, the regression curve of is acquired with the averaged AOD_mar at 532 nm for each wind speed grid and the surface wind speed which is up to $29\ \text{m}\cdot\text{s}^{-1}$, and the regression function is shown as the following Eq. 3:

$$\mathrm{AOD}_{\mathrm{mar},532} = \frac{0.15}{1+6.7\cdot e^{-0.17\cdot U_{10}}}, \quad (3)$$

where the U_{10} represents daily 10 m ocean surface wind speed.

As described above, the $\mathrm{AOD}_{\mathrm{mar}}$ data source (from spaceborne lidar observation), the study areas (remote ocean regions globally), and the wind speed range (0 $\mathrm{m\cdot s^{-1}}$ - 29 $\mathrm{m\cdot s^{-1}}$) of the $\mathrm{AOD}_{\mathrm{mar}}$ - ws relationship exploration in Kiliyanpilakkil and Meskhidze (2011) match well with those of this study. Hence, we select the $\mathrm{AOD}_{\mathrm{mar}}$ - ws relationship established by Kiliyanpilakkil and Meskhidze (2011) for the comparison. Additionally, due to the different wavelengths of $\mathrm{AOD}_{\mathrm{mar}}$ used in this study (355 nm) and in Kiliyanpilakkil and Meskhidze (2011) (532 nm), the effort on conversion of the $\mathrm{AOD}_{\mathrm{mar}}$ at 532 nm to the $\mathrm{AOD}_{\mathrm{mar}}$ at 355 nm is performed by applying the typical Ångström exponent of marine aerosol. It is reported that the marine aerosol Ångström exponent is surface wind speed related, and a linear relationship was established as the following Eq. 4 (Sayer et al., 2012):

$$A(ws)=0.69-0.030\cdot ws, \quad (4)$$

where A represents the Ångström exponent and ws represents the wind speed. Then the $\mathrm{AOD}_{\mathrm{mar}}$ at 532 nm can be converted to the $\mathrm{AOD}_{\mathrm{mar}}$ at 355 nm by the following Eq. 5:

$$\mathrm{AOD}_{\mathrm{mar},355\mathrm{nm}}(ws)=\exp[A(ws)\cdot\ln\frac{532}{355}]\cdot\mathrm{AOD}_{\mathrm{mar},532\mathrm{nm}}(ws) \ . \quad (5)$$

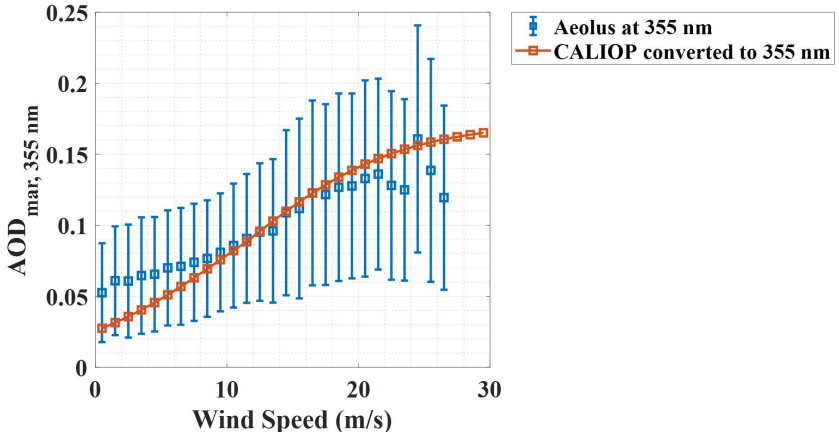

Figure 11: $\mathrm{AOD}_{\mathrm{mar}}$ at 355 nm versus wind speed. The blue squares and the corresponding error bars represent the $\mathrm{AOD}_{\mathrm{mar}}$ means and standard deviations along the ws grid of all the three study areas in this study; the red squares and line represent the $\mathrm{AOD}_{\mathrm{mar}}$ at 355 nm along the ws grid converted from the regressive relationship between the $\mathrm{AOD}_{\mathrm{mar}}$ at 532 nm and the ocean surface wind speed reported by Kiliyanpilakkil and Meskhidze (2011).

In Fig. 11, the averaged $\mathrm{AOD}_{\mathrm{mar}}$ and the corresponding standard deviations at 355 nm of all three study areas along the wind speed grid are represented as the blue squares and the error bars, while the regression curve of $\mathrm{AOD}_{\mathrm{mar}}$ at 355 nm versus

wind speed converted from Eq. 3 are represented as the red squares and line. Although instantaneous layer-averaged wind speed and daily ocean surface wind speed are used in this study and in Kiliyanpilakkil and Meskhidze (2011) individually, similar tendency of AOD_{mar} at 355 nm versus wind speed are obtained. It can be found that AOD_{mar} is increasing with wind speed, and the slope of AOD_{mar} turns out becoming higher along the wind speeds when the wind speed is below 15 $m \cdot s^{-1}$ while the variation of AOD_{mar} becomes slower above 15 $m \cdot s^{-1}$. The converted CALIOP AOD_{mar} are lower than the Aeolus retrieved AOD_{mar} at 0-10 $m \cdot s^{-1}$, nevertheless the formers are all in the standard deviations range of the latter, thus it is considered that the Aeolus retrieved AOD_{mar} and their variation along the wind speed are reasonable. The lower AOD_{mar} from CALIOP after wavelength conversion at low wind speed may arise from using a fixed LR_{mar} of 20 sr at 532 nm for CALIOP AOD_{mar} retrievals while the LR_{mar} can vary with a quite large range of 10 sr to 90 sr (Masonis et al., 2003). Possible uncertainties of the CALIOP retrieved AOD_{mar} at 532 nm is discussed in detail in Kiliyanpilakkil and Meskhidze (2011). Besides, as discussed in Section 4.4.2 of this paper, the particle size of marine aerosol and the LR_{mar} will vary with wind speed, so using the CALIOP AOD_{mar} retrieved with the fixed LR_{mar} may generate additional error in the exploration of the relationship between the AOD_{mar} and the wind speed. Therefore, using Aeolus retrieved AOD_{mar}, which is integrated by independently retrieved extinction coefficient without the assumption of LR_{mar}, could make the AOD_{mar} - *ws* relationship more reliable.

4.4.2 Marine aerosol lidar ratio vs. wind speed

As one of the intensive optical properties, LR_{mar} independent of the aerosol concentration. It is reported that the LR_{mar} depends on the particle size, and specifically, with the reduction of the coarse mode, the total LR turns out to increase (Masonis et al., 2003). The possible reason for this phenomenon is that as the particles become smaller, the extinction is enhanced by the increasing sideward scattering and the backscatter gets weaker due to the decrease of the scattering cross section (Haarig et al., 2017). Aeolus L2A product provide particle extinction-to-backscatter ratio calculated with the raw β, which lacks the depolarized portion, as introduced in Section 3 of this paper. In this work, the corrected LR_{mar} is acquired by dividing the marine aerosol extinction to the marine aerosol depolarization-corrected backscatter. The calculation of the averaged LR_{mar} along wind speed grid has been conducted by averaging the LR_{mar} s of each 1 $m \cdot s^{-1}$ wind speed bin, meanwhile the standard deviations are acquired as well. It should be noted that before the statistical calculation, the outliers are eliminated by the method of boxplot analysis, which is introduced in Section 3 of this paper.

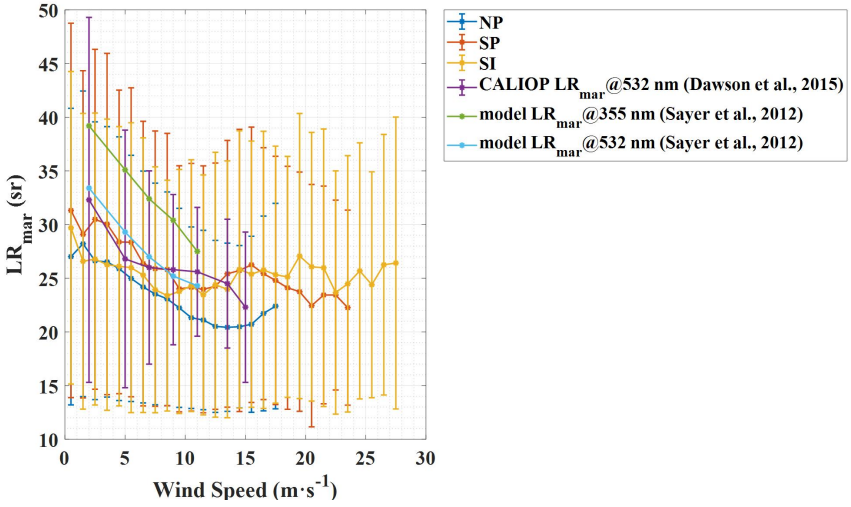

Figure 12: LR_{mar} **versus the wind speed. The dark blue curve, red curve, yellow curve and the corresponding error bars represent the averaged** LR_{mar} **and their standard deviations above the NP area, the SP area and the SI area, respectively. The purple curve and the corresponding error bars represent the CALIOP-retrieved** LR_{mar} **at 532 nm (Dawson et al., 2015). The green curve and the light blue curve represent the modeled** LR_{mar} **at 355 nm and at 532 nm, respectively (Sayer et al., 2012).**

In Fig. 12, 0-2 km averaged LR_{mar} variations along with the wind speed above the NP area, the SP area and the SI area are represented as the blue curve, the red curve and the yellow curve, respectively. Generally, the distinct downward trend of the LR_{mar} at relatively low wind speeds (0-14 $m \cdot s^{-1}$ of the NP area, 0-9 $m \cdot s^{-1}$ of the SP area and 0-10 $m \cdot s^{-1}$ of the SI area) can be observed in all cases. The results reported in this paper are similar to those in the previous studies, of which Dawson et al. (2015) and Sayer et al. (2012) investigated the relationship between LR_{mar} and wind speed utilizing measured LR_{mar} and modeled LR_{mar} respectively. Combining the corrected CALIOP-retrieved LR_{mar} at 532 nm and 10 m ocean surface wind speed from the AMSR-E, the negative correlation between the LR_{mar} and wind speed is acquired with the wind speed bins of 0 $m \cdot s^{-1}$ up to >15 $m \cdot s^{-1}$, shown as the purple curve in Fig. 12 (Dawson et al., 2015). The modeled LR_{mar} at 355 nm and at 532 nm also presents decreasing trends with the wind speed increases, presented as the green curve and the light blue curve in Fig. 12 (Sayer et al., 2012). These results seem to imply that as the wind speed increases for a low wind speed range, the particle size of marine aerosol get larger. The phenomenon is explained by the shift in marine aerosol volume size distribution with wind speed as wind speed increases, the fine mode volume size distribution of marine aerosol turns out decline while the coarse mode distribution becomes larger (Dawson et al., 2015; Smirnov et al., 2003; Sayer et al., 2012). The CALIOP LR_{mar} and the modeled LR_{mar} are all larger than the LR_{mar} of this study but are all in the standard deviation ranges. According to Groß et al. (2011), Groß et al. (2015), Bohlmann et al. (2018) and Floutsi et al. (2023), the pure LR_{mar} at 355 nm can vary from 10 sr to 40 sr, with the average of around 20 sr, thus it is considered that the averaged LR_{mar} in this

study are reasonable. At the middle wind speed range (14 $m \cdot s^{-1}$ -18 $m \cdot s^{-1}$ of the NP area, 9 $m \cdot s^{-1}$ -16 $m \cdot s^{-1}$ of the SP area, 10 $m \cdot s^{-1}$ -20 $m \cdot s^{-1}$ of the SI area), the LR_{mar} show upward tendencies, implying that the marine aerosol particles might be broken up into smaller ones with a wind speed increase. At the very high wind speed above the SP area (>16 $m \cdot s^{-1}$) and the SI area (>20 $m \cdot s^{-1}$), the LR_{mar} turns out decreasing with the wind speed again, which indicates that the particle size of marine aerosol becomes larger at this wind speed condition.

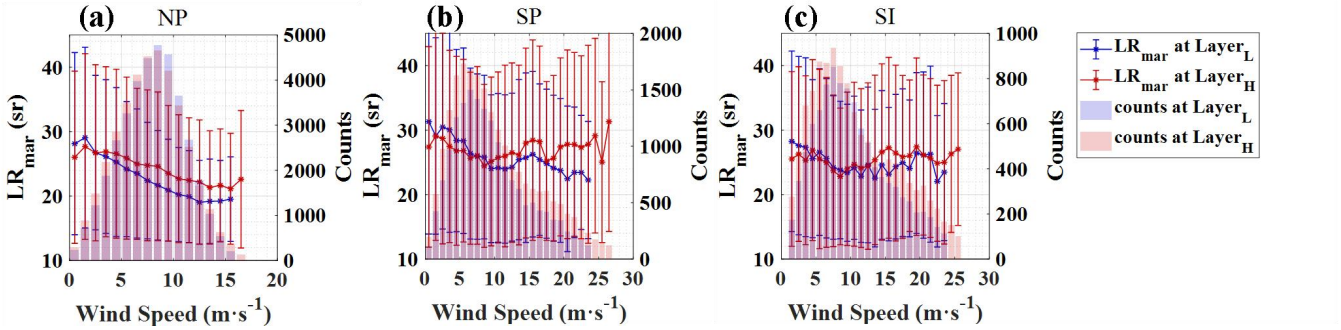

Figure 13: Averaged LR_{mar} versus wind speed at $Layer_L$ and $Layer_H$, in (a) the NP area, (b) the SP area and (c) the SI area, respectively.

Figure 13 shows the LR_{mar} variations at $Layer_L$ and $Layer_H$ along with the wind speed grid in three study areas. Some divergences of the LR_{mar} variations between the layers can be discovered. As for the NP area, the variation of LR_{mar} at $Layer_L$ is from 29 sr at 1-2 $m \cdot s^{-1}$ to 19 sr at 12-13 $m \cdot s^{-1}$, larger than that at $Layer_H$, which is from 28 sr at 1-2 $m \cdot s^{-1}$ to 21 sr at 15-16 $m \cdot s^{-1}$. Regarding to the SP area and the SI area, the downward trend of LR_{mar} at high wind speed condition as mentioned above is not apparent at $Layer_H$. Moreover, at $Layer_H$, the LR_{mar} can reach up to 27-28 sr at 15-25 $m \cdot s^{-1}$, close to that at 0-5 $m \cdot s^{-1}$, implying that the marine aerosol particle sizes at low and high wind speed are similar.

Generally, the LR_{mar} dependency along with the wind speed shows a downward trend at relatively low wind speed, then an upward trend at the middle wind speed, finally again a downward at the very high wind speed (if exist), which implies that the marine aerosol particle size is increasing along with the wind speed at first, then might be broken up into smaller one by the enhanced wind speed and ultimately turns out to a larger size again. Several differences of the LR_{mar} variations along with the wind speed appear between the three study areas and the two vertical layers, which may be due to the differences in meteorological and environmental conditions of the areas and the layers.

5 Summary and conclusion

By utilizing particle optical properties data (Level 2A products) and wind vector data (Level 2C products) provided by ALADIN, and L2 vertical feature mask (VFM) products provided by CALIOP, the optical properties at 355 nm of pure

marine aerosol are derived. The correlation between marine aerosol optical properties at 355 nm and the instantaneous co-located wind speed over remote ocean areas is investigated and discussed at two separate vertical atmospheric layers ($\mathrm{Layer_L}$ with the height of 0-1 km and $\mathrm{Layer_H}$ with the height of 1-2 km, corresponding to the heights within and above marine atmospheric boundary layer (MABL)), revealing the effect of wind speed on marine aerosol within and above the MABL over the remote oceans.

Three study areas located in remote ocean were selected, which were named the North Pacific (NP) area, the South Pacific (SP) area and the South Indian (SI) area, respectively. Then we examined the domination of marine aerosol with the aerosol classification data provided by CALIOP VFM products. The proportions of marine aerosol in these three areas are all larger than 79% respectively while the percentage sums of marine aerosol and dusty marine aerosol are all above 90%. After quality control, cloud screening was conducted with the criteria (relative humidity and backscatter ratio), and 9%, 35%, 40% data was identified cloud contaminated in the altitude range of 0-2 km then was eliminated for the NP area, the SP area and the SI area, respectively. Finally, backscatter correction is applied to the Aeolus L2A products. These procedures allow us to obtain reliable, cloud-free marine aerosol optical properties and the corresponding wind speed.

The correlation between the marine aerosol optical properties (extinction coefficient (α_{mar}) and backscatter coefficient (β_{mar})) at 355 nm and the wind speed (ws) are analysed at $\mathrm{Layer_L}$ and $\mathrm{Layer_H}$, for three study areas respectively. It is found that the observations of Aeolus can provide the evidence of the fact that the MABL will receive the marine aerosol produced and transported from the sea-air interface. Furthermore, the observations suggest that even the layer above the MABL may also receive the marine aerosol input. Moreover, the marine aerosol load at the lower layer (MABL) is stronger than at the higher layer. The marine aerosol extinction/backscatter coefficients' enhancements caused by the background wind are more intensive at the MABL. This may be due to the MABL's proximity to the sea-air interface, making it more susceptible to such effects. Besides, the slope variation points (15 $\mathrm{m \cdot s^{-1}}$ for α_{mar} and 10 $\mathrm{m \cdot s^{-1}}$ for β_{mar}) were found during α_{mar} and β_{mar} increasing with wind speed, above which the growth rates become lower. This phenomenon illustrate that the enhancement of marine aerosol driven by wind includes two phases, among them one is a rapid growth phase with high dependency of wind, and another is a slower growth phase with higher fluctuations after the slope variation points. The α_{mar} - ws curves and the β_{mar} - ws curves were fitted by power law functions and the corresponding R^2 are all higher than 0.9 for both layers above all three study areas. Regarding to the derived data, compared with the regression function between wavelength-converted CALIOP-retrieved $\mathrm{AOD_{mar}}$ and 10 m surface wind speed, the $\mathrm{AOD_{mar}}$ at 355 nm versus the wind speed in this work shows quite consistent tendency with CALIOP's though the wind speeds used are different. The $\mathrm{LR_{mar}}$ and marine aerosol particle size have negative relationship (Masonis et al., 2003). From the relationship between the $\mathrm{LR_{mar}}$ and the wind speed, it indicates that as the wind speed is increasing, the particle size of marine aerosol obviously becomes larger at relative low wind speed range, then could be broken up into smaller by wind at higher wind speed, and ultimately turns out a larger state again at very high wind speed. As aerosol optical properties are affected by both particle

concentration and size, this reminds us that the increase in α_{mar} and β_{mar} with wind speed may not only be due to the enhancement of particulate quantity produced from the sea-air interface, but may also be impacted by the size variation.

This study demonstrates Aeolus' ability to quantify interactions between aerosols and wind speeds in poorly observed ocean regions through a synergy of aerosol and wind observations. The α_{mar} - ws , β_{mar} - ws models within and above MABL at remote ocean areas were established with Aeolus provided data. These models deepens our understanding of the correlation between marine aerosol optical properties and wind in remote ocean areas across two vertical layers based on the unique setup and the ability to deliver winds of Aeolus observations. Nevertheless, the regression curves of α_{mar} - ws and β_{mar} - ws above three study areas (the NP area, located in the Pacific Ocean, the low latitudes of the Northern Hemisphere; the SP area, located in the Pacific Ocean, the middle latitudes of the Southern Hemisphere; the SI area, located in the Indian Ocean, the middle latitudes of the Southern Hemisphere) are inconsistent, while the meteorological and environmental parameters, apart from wind, differ across various regions. It implies that the relationships between marine aerosol optical properties and wind speed are more complex than a linear or exponential relation. In order to obtain more precise α_{mar} and β_{mar} models, besides wind speed, other meteorological and environmental factors, e.g., atmospheric stability, sea and air temperature, RH, etc. should participate in the establishment of the models, because the production, entrainment, transport and removal of the marine aerosol above the ocean are not only dominated by the wind, but also be impacted by these factors (Lewis and Schwartz, 2004).

Data availability

The Aeolus data are downloaded via the website https://aeolus-ds.eo.esa.int/oads/access/collection (last access: 9 March 2023). Part of the Aeolus L2A and L2C data we used in this paper are not available publicly at the time the article was submitted. We are allowed to access the data through our participation as a Calibration and Validation team. The CALIOP data can be downloaded from https://eosweb.larc.nasa.gov/project/CALIPSO (last access: 9 March 2023).

Author contributions

G. Dai conceived of the idea for correlation between marine aerosol optical properties and wind fields over remote oceans with spaceborne lidars ALADIN, CALIOP; K. Sun wrote the manuscript; K. Sun, G. Dai, S. Wu, O. Reitebuch and H. Baars contributed to the data analyses; J. Liu and S. Zhang contributed to the scientific discussion. All the co-authors reviewed and edited the manuscript.

Competing interests

The authors declare that they have no conflict of interest.

Special issue statement

This article is part of the special issue “Aeolus data and their application”. It is not associated with a conference.

Acknowledgments

This study has been jointly supported by the Laoshan Laboratory Science and Technology Innovation Projects under grant LSKJ202201406, the National Natural Science Foundation of China (NSFC) under grant 61975191, 41905022 and U2106210. This work was also supported by Dragon 5 program which conducted by European Space Agency (ESA) and the National Remote Sensing Center of China (NRSCC) under grant 59089.

References

Abril-Gago, J., Guerrero-Rascado, J. L., Costa, M. J., Bravo-Aranda, J. A., Sicard, M., Bermejo-Pantaleón, D., Bortoli, D., Granados-Muñoz, M. J., Rodríguez-Gómez, A., Muñoz-Porcar, C., Comerón, A., Ortiz-Amezcua, P., Salgueiro, V., Jiménez-Martín, M. M., and Alados-Arboledas, L.: Statistical validation of Aeolus L2A particle backscatter coefficient retrievals over ACTRIS/EARLINET stations on the Iberian Peninsula, Atmos. Chem. Phys., 22, 1425–1451, https://doi.org/10.5194/acp-22-1425-2022, 2022.

Adames, A. F., Reynolds, M., Smirnov, A., Covert, D. S., and Ackerman, T. P.: Comparison of MODIS ocean aerosol retrievals with ship-based sun photometer measurements from the “Around the America’s” expedition, J. Geophys. Res., 116, D16303, https://doi.org/10.1029/2010JD015440, 2011.

Alexander, S. P. and Protat, A.: Vertical profiling of aerosols with a combined Raman-elastic backscatter lidar in the remote Southern Ocean marine boundary layer (43–66°S, 132–150°E), J. Geophys. Res.-Atmos., 124, 12107–12125, https://doi.org/10.1029/2019JD030628, 2019.

Ansmann, A., Wandinger, U., Le Rille, O., Lajas, D., and Straume, A. G.: Particle backscatter and extinction profiling with the spaceborne high-spectral-resolution Doppler lidar ALADIN: methodology and simulations, Appl. Optics, 46, 6606, https://doi.org/10.1364/AO.46.006606, 2007.

Baars, H., Radenz, M., Floutsi, A. A., Engelmann, R., Althausen, D., Heese, B., Ansmann, A., Flament, T., Dabas, A., Trapon, D., Reitebuch, O., Bley, S., and Wandinger, U.: Californian wildfire smoke over Europe: A first example of the aerosol observing capabilities of Aeolus compared to ground-based lidar, Geophysical Research Letters, 48, e2020GL092194. https://doi.org/10.1029/2020GL092194, 2021.

Bohlmann, S., Baars, H., Radenz, M., Engelmann, R., and Macke, A.: Ship-borne aerosol profiling with lidar over the Atlantic Ocean: from pure marine conditions to complex dust–smoke mixtures, Atmos. Chem. Phys., 18, 9661–9679, https://doi.org/10.5194/acp-18-9661-2018, 2018.

Boucher, O., D. Randall, P. Artaxo, C. Bretherton, G. Feingold, P. Forster, V.-M. Kerminen, Y. Kondo, H. Liao, U. Lohmann, P. Rasch, S.K. Satheesh, S. Sherwood, B. Stevens and X.Y. Zhang, 2013: Clouds and Aerosols. In: Climate Change 2013: The Physical Science Basis. Contribution of Working Group I to the Fifth Assessment Report of the Intergovernmental Panel on Climate Change [Stocker, T.F., D. Qin, G.-K. Plattner, M. Tignor, S.K. Allen, J. Boschung, A. Nauels, Y. Xia, V. Bex and P.M. Midgley (eds.)]. Cambridge University Press, Cambridge, United Kingdom and New York, NY, USA.

Dabas, A., Denneulin, M. L., Flamant, P., Loth, C., Garnier, A., and Dolfi-Bouteyre, A.: Correcting winds measured with a Rayleigh Doppler lidar from pressure and temperature effects, Tellus A, 60, 206–215, https://doi.org/10.1111/j.1600-0870.2007.00284.x, 2008.

Dai, G., Sun, K., Wang, X., Wu, S., E, X., Liu, Q., and Liu, B.: Dust transport and advection measurement with spaceborne lidars ALADIN and CALIOP and model reanalysis data, Atmos. Chem. Phys., 22, 7975–7993, https://doi.org/10.5194/acp-22-7975-2022, 2022.

de Leeuw, G., Neele, F. P., Hill, M., Smith, M. H., and Vignati, E.: Production of sea spray aerosol in the surf zone, J. Geophys. Res., 105, 29397-29409, https://doi.org/10.1029/2000JD900549, 2000.

Dawson, K. W., Meskhidze, N., Josset, D., and Gassó, S.: Spaceborne observations of the lidar ratio of marine aerosols, Atmos. Chem. Phys., 15, 3241–3255, https://doi.org/10.5194/acp-15-3241-2015, 2015.

Fan, T. and Toon, O. B.: Modeling sea-salt aerosol in a coupled climate and sectional microphysical model: mass, optical depth and number concentration, Atmos. Chem. Phys., 11, 4587-4610, https://doi.org/10.5194/acp-11-4587-2011, 2011.

Flamant, P. H., Cuesta, J., Denneulin, M.-L., Dabas, A., and Huber, D.: ADM-Aeolus retrieval algorithms for aerosol and cloud products, Tellus A, 60, 273–286, https://doi.org/10.1111/j.1600-0870.2007.00287.x, 2008.

Flamant, P. H., Lever, V., Martinet, P., Flament, T., Cuesta, J., Dabas, A., Olivier, M., Huber, D., Trapon, D., and Lacour, A.: Aeolus Level-2A Algorithm Theoretical Basis Document, version 5.7, https://earth.esa.int/eogateway/documents/20142/37627/Aeolus-L2A-Algorithm-Theoretical-Baseline-Document (last access: 9 November 2022), 2020.

Flament, T., Trapon, D., Lacour, A., Dabas, A., Ehlers, F., and Huber, D.: Aeolus L2A aerosol optical properties product: standard correct algorithm and Mie correct algorithm, Atmos. Meas. Tech., 14, 7851–7871, https://doi.org/10.5194/amt-14-7851-2021, 2021.

Floutsi, A. A., Baars, H., Engelmann, R., Althausen, D., Ansmann, A., Bohlmann, S., Heese, B., Hofer, J., Kanitz, T., Haarig, M., Ohneiser, K., Radenz, M., Seifert, P., Skupin, A., Yin, Z., Abdullaev, S. F., Komppula, M., Filioglou, M., Giannakaki, E., Stachlewska, I. S., Janicka, L., Bortoli, D., Marinou, E., Amiridis, V., Gialitaki, A., Mamouri, R.-E., Barja, B., and Wandinger, U.: DeLiAn – a growing collection of depolarization ratio, lidar ratio and Ångström exponent for different aerosol types and mixtures from ground-based lidar observations, Atmos. Meas. Tech., 16, 2353–2379, https://doi.org/10.5194/amt-16-2353-2023, 2023.

Glantz, P., Nilsson, E. D., and von Hoyningen-Huene, W.: Estimating a relationship between aerosol optical thickness and surface wind speed over the ocean, Atmos. Res., 92, 58-68, https://doi.org/10.1016/j.atmosres.2008.08.010, 2009.

Grandey, B. S., Stier, P., Wagner, T. M., Grainger, R. G., and Hodges, K. I.: The effect of extratropical cyclones on satellite-retrieved aerosol properties over ocean, Geophys. Res. Lett., 38, L13805, https://doi.org/10.1029/2011GL047703, 2011.

Groß, S., Tesche, M., Freudenthaler, V., Toledano, C., Wiegner, M., Ansmann, A., Althausen, D. and Seefeldner, M.: Characterization of Saharan dust, marine aerosols and mixtures of biomass-burning aerosols and dust by means of multi-wavelength depolarization and Raman lidar measurements during SAMUM 2, Tellus B: Chemical and Physical Meteorology, 63(4), 706–724, http://doi.org/10.1111/j.1600-0889.2011.00556.x, 2011

Groß, S., Esselborn, M., Weinzierl, B., Wirth, M., Fix, A., and Petzold, A.: Aerosol classification by airborne high spectral resolution lidar observations, Atmos. Chem. Phys., 13, 2487–2505, https://doi.org/10.5194/acp-13-2487-2013, 2013.

Groß, S., Freudenthaler, V., Wirth, M., and Weinzierl, B.: Towards an aerosol classification scheme for future EarthCARE lidar observations and implications for research needs, Atmos. Sci. Lett., 16: 77-82, https://doi.org/10.1002/asl2.524, 2015.

Haarig, M., Ansmann, A., Gasteiger, J., Kandler, K., Althausen, D., Baars, H., Radenz, M., and Farrell, D. A.: Dry versus wet marine particle optical properties: RH dependence of depolarization ratio, backscatter, and extinction from multiwavelength lidar measurements during SALTRACE, Atmos. Chem. Phys., 17, 14199–14217, https://doi.org/10.5194/acp-17-14199-2017, 2017.

Haywood, J. M., V. Ramaswamy, and B. J. Soden: Tropospheric aerosol climate forcing in clear-sky satellite observations over the oceans, Science, 283, 1299-1303, https://doi.org/10.1126/science.283.5406.1299, 1999.

Hoaglin, D. C., Iglewicz, B., and Tukey, J. W.: Performance of some resistant rules for outlier labelling, Journal of the American Statistical Association, 81(396), 991-999, https://doi.org/10.1080/01621459.1986.10478363, 1986.

Huang, H., Thomas, G. E., and Grainger, R. G.: Relationship between wind speed and aerosol optical depth over remote ocean, Atmos. Chem. Phys., 10, 5943-5950, https://doi.org/10.5194/acp-10-5943-2010, 2010.

IPCC, 2021: Summary for Policymakers. In: Climate Change 2021: The Physical Science Basis. Contribution of Working Group I to the Sixth Assessment Report of the Intergovernmental Panel on Climate Change [Masson-Delmotte, V., P. Zhai, A. Pirani, S.L. Connors, C. Péan, S. Berger, N. Caud, Y. Chen, L. Goldfarb, M.I. Gomis, M. Huang, K. Leitzell, E. Lonnoy, J.B.R. Matthews, T.K. Maycock, T. Waterfield, O. Yelekçi, R. Yu, and B. Zhou (eds.)]. Cambridge University Press, Cambridge, United Kingdom and New York, NY, USA, 3-32, doi:10.1017/9781009157896.001.

Jaegle, L., Quinn, P. K., Bates, T., Alexander, B., and Lin, J.-T.: Global distribution of sea salt aerosols: new constraints from in situ and remote sensing observations, Atmos. Chem. Phys., 11, 3137-3157, https://doi.org/10.5194/acp-11-3137-2011, 2011.

Josset, D., Pelon, J., Protat, A., and Flamant, C.: New approach to determine aerosol optical depth from combined CALIPSO and CloudSat ocean surface echoes, Geophys. Res. Lett., 35, L10805, https://doi.org/10.1029/2008GL033442, 2008.

Kahn, R. A., Gaitley, B. J., Garay, M. J., Diner, D. J., Eck, T. F., Smirnov, A., and Holben, B. N.: Multiangle Imaging SpectroRadiometer global aerosol product assessment by comparison with the Aerosol Robotic Network, J. Geophys. Res., 115, D23209, https://doi.org/10.1029/2010JD014601, 2010.

Kanitz, T., Lochard, J., Marshall, J., McGoldrick, P., Lecrenier, O., Bravetti, P., Reitebuch, O., Rennie, M., Wernham, D., and Elfving, A.: Aeolus first light: first glimpse, International Conference on Space Optics–ICSO 2018, 111801R, Chania, Greece, 9–12 October 2018, https://doi.org/10.1117/12.2535982, 2019.

Kaufman, Y. J., D. Tanre, and O. Boucher: A satellite view of aerosols in the climate system, Nature, 419, 215-223, https://doi.org/10.1038/nature01091, 2002.

Kiliyanpilakkil, V. P. and Meskhidze, N.: Deriving the effect of wind speed on clean marine aerosol optical properties using the A-Train satellites, Atmos. Chem. Phys., 11, 11401–11413, https://doi.org/10.5194/acp-11-11401-2011, 2011.

Kim, M.-H., Omar, A. H., Tackett, J. L., Vaughan, M. A., Winker, D. M., Trepte, C. R., Hu, Y., Liu, Z., Poole, L. R., Pitts, M. C., Kar, J., and Magill, B. E.: The CALIPSO version 4 automated aerosol classification and lidar ratio selection algorithm, Atmos. Meas. Tech., 11, 6107–6135, https://doi.org/10.5194/amt-11-6107-2018, 2018.

Kleidman, R. G., Smirnov, A., Levy, R. C., Mattoo, S., and Tanre, D.: Evaluation and wind speed dependence of MODIS aerosol retrievals over open ocean, IEEE T. Geosci. Remote, 50, 429-435, https://doi.org/10.1109/TGRS.2011.2162073, 2012.

Labzovskii, L. D., van Zadelhoff, G. J., Tilstra, L. G., de Kloe, J., Donovan, D. P., and Stoffelen, A.: High sensitivity of Aeolus UV surface returns to surface reflectivity, Sci. Rep., 13, 17552, https://doi.org/10.1038/s41598-023-44525-5, 2023.

Latham, J., and M. H. Smith: Effect on global warming of wind-dependent aerosol generation at the ocean surface, Nature, 347, 372-373, https://doi.org/10.1038/347372a0, 1990.

Lehahn, Y., Koren, I., Boss, E., Ben-Ami, Y., and Altaratz, O.: Estimating the maritime component of aerosol optical depth and its dependency on surface wind speed using satellite data, Atmos. Chem. Phys., 10, 6711-6720, https://doi.org/10.5194/acp-10-6711-2010, 2010.

Lewis, R. and Schwartz, E.: Sea salt aerosol production: mechanisms, methods, measurements and models – a critical review, American Geophysical Union, https://doi.org/10.1029/GM152, 2004.

Liu, Z., Kar, J., Zeng, S., Tackett, J., Vaughan, M., Avery, M., Pelon, J., Getzewich, B., Lee, K.-P., Magill, B., Omar, A., Lucker, P., Trepte, C., and Winker, D.: Discriminating between clouds and aerosols in the CALIOP version 4.1 data products, Atmos. Meas. Tech., 12, 703–734, https://doi.org/10.5194/amt-12-703-2019, 2019.

Luo, T., Yuan, R., and Wang, Z.: Lidar-based remote sensing of atmospheric boundary layer height over land and ocean, Atmos. Meas. Tech., 7, 173–182, https://doi.org/10.5194/amt-7-173-2014, 2014.

Luo, T., Wang, Z., Zhang, D., and Chen, B.: Marine boundary layer structure as observed by A-train satellites, Atmos. Chem. Phys., 16, 5891–5903, https://doi.org/10.5194/acp-16-5891-2016, 2016.

Madry, W. L., Toon, O. B., and O'Dowd, C. D.: Modeled optical thickness of sea salt aerosol, J. Geophys. Res., 116, D08211, https://10.1029/2010JD014691, 2011.

Masonis, S. J., Anderson, T. L., Covert, D. S., Kapustin, V., Clarke, A. D., Howell, S., and Moore, K.: A study of the extinction-to-backscatter ratio of marine aerosol during the Shoreline Environment Aerosol Study, J. Atmos. Ocean. Tech., 20, 1388–1402, https://10.1175/1520-0426(2003)020<1388:ASOTER>2.0.CO;2, 2003.

Meskhidze, N. and Nenes, A.: Effects of ocean ecosystem on marine aerosol-cloud interaction, Adv. Meteorol., 2010, 239808, https://10.1155/2010/239808, 2010.

Mulcahy, J. P., O'Dowd, C. D., Jennings, S. G., and Ceburnis, D.: Significant enhancement of aerosol optical depth in marine air under wind conditions, Geophys. Res. Lett., 35, L16810, https://10.1029/2008GL034303, 2008.

Murphy, D. M., Anderson, J. R., Quinn, P. K., Mcinnes, L. M., Brechtel, F. J., Kreidenweis, S. M., Middlebrook, A. M., Pósfai, M., Thomson, D. S., and Buseck, P. R.: Influence of sea-salt on aerosol radiative properties in the Southern Ocean marine boundary layer, Nature, 392, 62-65, https://doi.org/10.1038/32138, 1998.

O'Dowd, C. D. and de Leeuw, G.: Marine aerosol production: a review of the current knowledge, Phil. Trans. R. Soc, 365, 1753-1774, https://doi.org/10.1098/rsta.2007.2043, 2007.

O'Dowd, C. D., Lowe, J. A., and Smith, M. H.: Coupling sea-salt and sulphate interactions and its impact on cloud droplet concentration predications, Geophys. Res. Lett., 26, 1311-1314, https://10.1029/1999GL900231, 1999.

O'Dowd, C. D., Scannell, C., Mulcahy, J., and Jennings, S. G.: Wind speed influences on marine aerosol optical depth, Adv. Meteorol., 2010, 830846, https://10.1155/2010/830846, 2010.

Pierce, J. R. and Adams, P. J.: Global evaluation of CCN formation by direct emission of sea salt and growth of ultrafine sea salt, J. Geophys. Res., 111, D06203, https://10.1029/2005JD006186, 2006.

Platt, C. M. R. and G. R. Patterson: The interpretation of baseline atmospheric turbidity measurements at Cape Grim, Tasmania, Journal of Atmospheric Chemistry, 4, 187-197, https://10.1007/BF00053778, 1986.

Prijith, S. S., Aloysius, M., and Mohan, M.: Relationship between wind speed and sea salt aerosol production: A new approach, Journal of Atmospheric and Solar-Terrestrial Physics, 108, 34-40, https://10.1016/j.jastp.2013.12.009, 2014.

Reitebuch, O.: The spaceborne wind lidar mission ADM-Aeolus, in: Atmospheric Physics, edited by: Schumann, U., Springer, 815-827, ISBN 978-3-642-30182-7, https://doi.org/10.1007/978-3-642-30183-4_49, 2012.

Rennie, M., Tan, D., Andersson, E., Poli, P., Dabas, A., de Kloe, J., Marseille, G., and Stoffelen, A.: Aeolus Level-2B Algorithm Theoretical Basis Document, version 3.40, https://earth.esa.int/eogateway/documents/20142/37627/Aeolus-L2B-Algorithm-ATBD.pdf (last access: 7 November 2022), 2020.

Rennie, M. P., Isaksen, L., Weiler, F., de Kloe, J., Kanitz, T., and Reitebuch, O.: The impact of Aeolus wind retrievals on ECMWF global weather forecasts, Q. J. Roy. Meteor. Soc., 147, 3555–3586, https://doi.org/10.1002/qj.4142, 2021.

Sayer, A. M., Smirnov, A., Hsu, N. C., and Holben, B. N.: A pure marine aerosol model, for use in remote sensing applications, J. Geophys. Res., https://10.1029/2011JD016689, 2012.

Shin, D. H., Müller, D., Choi, T., Noh, Y. M., Yoon, Y. J., Lee, K. H., Shin, S. K., Chae, N., Kim, K., and Kim, Y. J.: Influence of wind speed on optical properties of aerosols in the marine boundary layer measured by ship-borne

DePolarization Lidar in the coastal area of Korea, Atmospheric Environment, 83, 282-290, https://10.1016/j.atmosenv.2013.10.027, 2014.

Shinozuka, Y., Clarke, A. D., Howell, S. G., Kapustin, V. N., and Huebert, B. J.: Sea-salt vertical profiles over the Southern and tropical Pacific oceans: Microphysics, optical properties, spatial variability, and variations with wind speed, J. Geophys. Res., 109, D24201, https://10.1029/2004JD004975, 2004.

Smirnov, A., Villevalde, Y., O'Neill, N. T., Royer, A., and Tarussov, A.: Aerosol optical depth over the oceans: Analysis in terms of synoptic air mass types, J. Geophys. Res., 100, 16639-16650, https://10.1029/95JD01265, 1995.

Smirnov, A., Holben, B. N., Eck, T. F., Dubovik, O., and Slutsker, I.: Effect of wind speed on columnar aerosol optical properties at Midway Island, J. Geophys. Res., 108, 4802, https://10.1029/2003JD003879, 2003.

Smirnov, A., Sayer, A. M., Holben, B. N., Hsu, N. C., Sakerin, S. M., Macke, A., Nelson, N. B., Courcoux, Y., Smyth, T. J., Croot, P., Quinn, P. K., Sciare, J., Gulev, S. K., Piketh, S., Losno, R., Kinne, S., and Radionov, V. F.: Effect of wind speed on aerosol optical depth over remote oceans, based on data from the Maritime Aerosol Network, Atmos. Meas. Tech., 5, 377–388, https://doi.org/10.5194/amt-5-377-2012, 2012.

Stoffelen, A., Pailleux, J., Källén, E., Vaughan, J. M., Isaksen, L., Flamant, P., Wergen, W., Andersson, E., Schyberg, H., and Culoma, A.: The atmospheric dynamics mission for global wind field measurement, B. Am. Meteorol. Soc., 86, 73–88, https://doi.org/10.1175/BAMS-86-1-73, 2005.

Tan, D. G., Andersson, E., Kloe, J. D., Marseille, G.-J., Stoffelen, A., Poli, P., Denneulin, M.-L., Dabas, A., Huber, D., and Reitebuch, O.: The ADM-Aeolus wind retrieval algorithms, Tellus A, 60, 191–205, https://doi.org/10.1111/j.1600-0870.2007.00285.x, 2008.

Reitebuch, O.: The Spaceborne Wind Lidar Mission ADM-Aeolus, in: Atmospheric Physics, Research Topics in Aerospace, edited by: Schumann, U., ISBN 978-3-642-30182-7, Springer-Verlag Berlin Heidelberg, 815–827, https://doi.org/10.1007/978-3-642-30183-4_49, 2012.

Trapon, D., Flament, T., Lacour, A. and Stieglitz, H.: L2A user guide, issue V 2.1, https://earth.esa.int/eogateway/documents/20142/37627/Aeolus-Data-Innovation-Science-Cluster-DISC-Level-2A-user-guide.pdf (last access: 27 Feburary 2023), 2022.

Villevalde, Yu. V., Smirnov, A. V., O'Neill, N. T., Smyshlyaev, S. P., and Yakovlev, V. V.: Measurement of aerosol optical depth in the Pacific Ocean and the North Atlantic, J. Geophys. Res., 99, 20983-20988, https://10.1029/94JD01618, 1994.

Wilson, S. R., and Forgan, B. W.: Aerosol optical depth at Cape Grim, Tasmania, 1986-1999, J. Geophys. Res., 107, D8, https://10.1029/2001JD000398, 2002.

Winker, D. M. and Pelon, J.: The CALIPSO mission, Geoscience and Remote Sensing Symposium, IGARSS '03, Proceedings, IEEE International, 2, 1329-1331, https://10.1109/IGARSS.2003.1294098, 2003.

Winker, D. M., Vaughan, M. A., Omar, A., Hu, Y., Powell, K. A., Liu, Z., Hunt, W. H., and Young, S. A.: Overview of the CALIPSO mission and CALIOP data processing algorithms, J. Atmos. Ocean. Tech., 26, 2310–2323, https://doi.org/10.1175/2009JTECHA1281.1, 2009.

Wu, S., Sun, K., Dai, G., Wang, X., Liu, X., Liu, B., Song, X., Reitebuch, O., Li, R., Yin, J., and Wang, X.: Inter-comparison of wind measurements in the atmospheric boundary layer and the lower troposphere with Aeolus and a ground-based coherent Doppler lidar network over China, Atmos. Meas. Tech., 15, 131–148, https://doi.org/10.5194/amt-15-131-2022, 2022.

Zibordi, G., Berthon, J.-F., Melin, F., and D'Alimonte, D.: Cross-site consistent in situ measurements for satellite ocean color applications: The BiOMaP radiometric dataset, Remote Sens. Env., 115, 2104-2115, https://doi.org/10.1016/j.rse.2011.04.013, 2011.